NAVAL POSTGRADUATE SCHOOL
MONTEREY, CALIFORNIA

THESIS

EFFECTS OF SHALLOW WATER BOTTOM INTERFACE ROUGHNESS AND VOLUME FLUCTUATIONS ON BROADBAND PULSE RESOLUTION

by

Mei-Chun Yuan

June, 1996

Principal Advisor: Kevin B. Smith
Second Reader: Anthony A. Atchley

Approved for public release; distribution is unlimited.

DISCLAIMER NOTICE

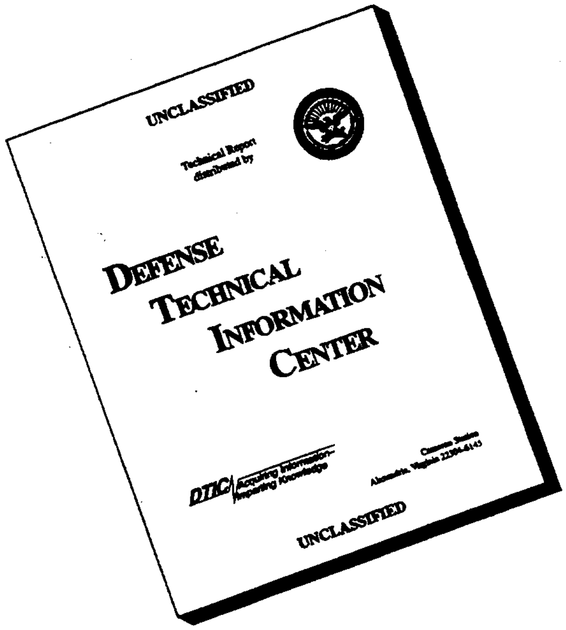

THIS DOCUMENT IS BEST QUALITY AVAILABLE. THE COPY FURNISHED TO DTIC CONTAINED A SIGNIFICANT NUMBER OF PAGES WHICH DO NOT REPRODUCE LEGIBLY.

REPORT DOCUMENTATION PAGE

Form Approved OMB No. 0704-0188

1. AGENCY USE ONLY *(Leave blank)*	2. REPORT DATE June 1996	3. REPORT TYPE AND DATES COVERED Master's Thesis

4. TITLE AND SUBTITLE EFFECTS OF SHALLOW WATER BOTTOM INTERFACE ROUGHNESS AND VOLUME FLUCTUATIONS ON BROADBAND PULSE RESOLUTION

5. FUNDING NUMBERS

6. AUTHOR(S) Mei-Chun Yuan

7. PERFORMING ORGANIZATION NAME(S) AND ADDRESS(ES)
Naval Postgraduate School
Monterey, CA 93943-5000

8. PERFORMING ORGANIZATION REPORT NUMBER

9. SPONSORING/MONITORING AGENCY NAME(S) AND ADDRESS(ES)

10. SPONSORING/MONITORING AGENCY REPORT NUMBER

11. SUPPLEMENTARY NOTES The views expressed in this thesis are those of the author and do not reflect the official policy or position of the Department of Defense or the U.S. Government.

12a. DISTRIBUTION/AVAILABILITY STATEMENT
Approved for public release; distribution is unlimited.

12b. DISTRIBUTION CODE

13. ABSTRACT *(maximum 200 words)*

Typical acoustic propagation in shallow water environments is dominated by bottom-interacting paths. The effects of rough bottom interfaces and sediment volume fluctuations are investigated using model simulations. A numerical study of low-frequency (~200 Hz) broadband pulse propagation is presented and several characterizations of bottom factors are examined. In particular, the variations of the interface rms roughness and a volume fluctuation strength constant on the time resolution of the broadband pulse are investigated. It is shown that interface roughness is the dominant factor in the degradation of pulse resolution.

14. SUBJECT TERMS Underwater Acoustic Propagation, PE Model, Beamforming, Pulse Resolution, Scattering.

15. NUMBER OF PAGES 67

16. PRICE CODE

17. SECURITY CLASSIFICATION OF REPORT Unclassified	18. SECURITY CLASSIFICATION OF THIS PAGE Unclassified	19. SECURITY CLASSIFICATION OF ABSTRACT Unclassified	20. LIMITATION OF ABSTRACT UL

NSN 7540-01-280-5500

Standard Form 298 (Rev. 2-89)
Prescribed by ANSI Std. 239-18 298-102

EFFECTS OF SHALLOW WATER BOTTOM INTERFACE ROUGHNESS AND VOLUME FLUCTUATIONS ON BROADBAND PULSE RESOLUTION

Mei-Chun Yuan
Lieutenant Commander, Republic of China Navy
B.S., Chung Cheng Institute of Technology - 1987

Submitted in partial fulfillment
of the requirements for the degree of

MASTER OF SCIENCE
IN
ENGINEERING ACOUSTICS

from the

NAVAL POSTGRADUATE SCHOOL
June 1996

Author: Mei-Chun Yuan
Mei-Chun Yuan

Approved by: Kevin B. Smith
Kevin B. Smith, Principal Advisor

Anthony A. Atchley
Anthony A. Atchley, Second Reader

Anthony A. Atchley
Anthony A. Atchley, Chairman
Engineering Acoustics Academic Committee

ABSTRACT

Typical acoustic propagation in shallow water environments is dominated by bottom-interacting paths. The effects of rough bottom interfaces and sediment volume fluctuations are investigated using model simulations. A numerical study of low-frequency (~200 Hz) broadband pulse propagation is presented and several characterizations of bottom factors are examined. In particular, the variations of the interface rms roughness and a volume fluctuation strength constant on the time resolution of the broadband pulse are investigated. It is shown that interface roughness is the dominant factor in the degradation of pulse resolution.

TABLE OF CONTENTS

LIST OF FIGURES

LIST OF TABLES

I. INTRODUCTION

Over the past few years, the interest in littoral, shallow water environments has increased significantly. The success of many naval systems in these environments depends on our ability to predict and interpret shallow water acoustic propagation. The sound speed profile in shallow water typically consists of an upper mixed layer below which the sound speed decreases to the bottom. Typical shallow-water environments are found on the continental shelf with approximate depths of 200 m. The wave propagation is downward refracting, that is, bottom-interacting paths dominate in long-range propagation as depicted in Figures 1 and Figure 2. Etter (1991) summarized the effect of the sea floor as:

- forward scattering and reflection loss (but complicated by refraction in the bottom);
- interference and frequency effects;
- attenuation by sediments;
- noise generation at lower frequencies due to seismic activity;
- backscattering and bottom reverberation.

The purpose of this thesis is to quantify the influence of bottom variability on the resolution of pulse transmissions in simple, shallow water environments.

Rough bottom interfaces can be modeled by assuming some realistic form of the spectral shape. The forward scatter of the acoustic field can then be treated deterministically. Fluctuations of the sediment properties, such as porosity, density, permeability, and shear strength, determine the sound scattering from the bottom volume. Yamamoto (1995) summarized the relationship between spectral strength and sediment type. We used this information to generate random two-dimensional wave-number spectra of the velocity variability in order to simulate a realistic ocean sediment volume. These techniques are described in more detail in Chapter II.

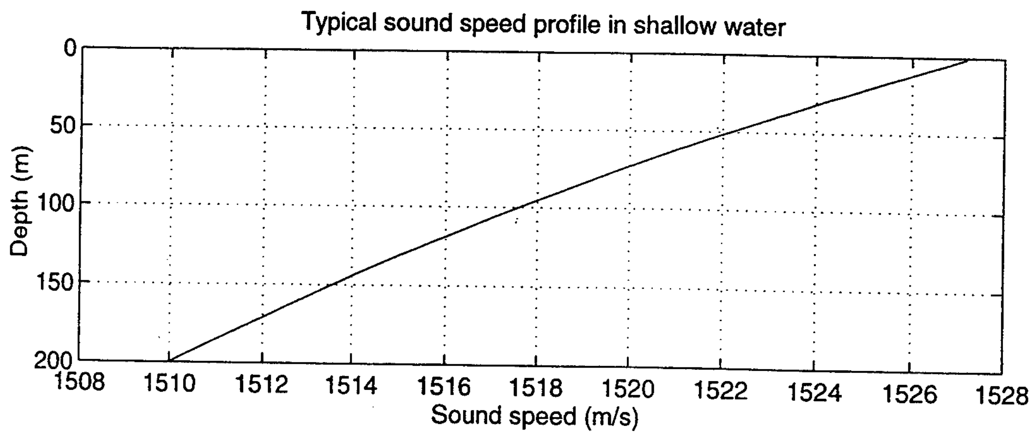

Figure 1. Typical sound speed profile in shallow water.

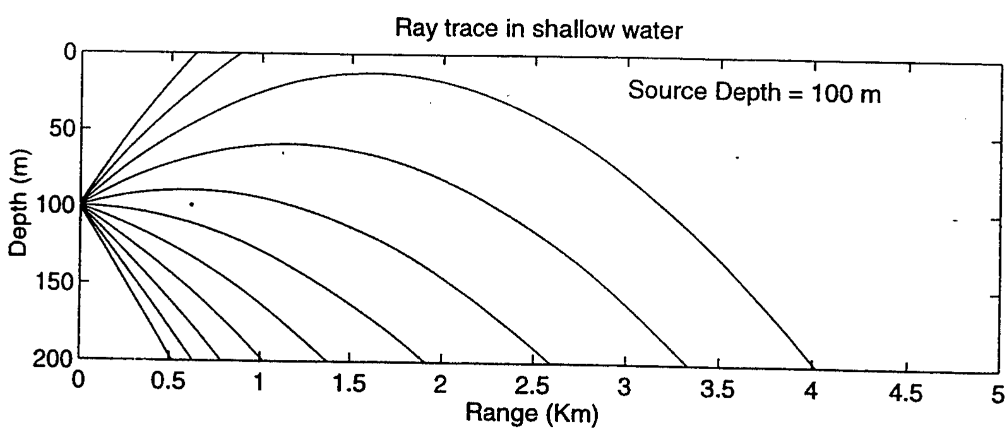

Figure 2. Ray trace in shallow water.

Wave propagation in an inhomogeneous medium is defined by the wave equation. The solution can be obtained by several approximate methods, for example, Wentzel-Kramers-Brillouin (WKB) approximation, ray approximation or parabolic equation approximation. The last method was used throughout this thesis study. Over the past few decades, ocean acoustic models have been developed and improved to analyze measured data and simulate sound propagation in real ocean environments. Modeling provides an efficient means by which to parametrically investigate the projector (source) radiated sound pattern under the influence of environmental conditions. A perfect model is one that perfectly represents reality. In practice, such a perfect model would be as complex as the problem it is attempting to represent. So, there are some assumptions built into every computer model. This thesis uses a version of the PE model developed at the University of Miami known as UMPE (Smith and Tappert, 1994).

In order to investigate the effects of bottom interface roughness and volume fluctuations, we simulate broadband pulse propagation for four different scenarios as follows:

- flat bottom with homogeneous sediment;
- rough bottom interface with homogeneous sediment;
- flat bottom interface with realistic sediment sound speed fluctuations; and
- rough bottom interface with realistic sediment sound speed fluctuations.

II. BACKGROUND

A. THE ACOUSTIC MODEL

Because propagation ranges are typically much larger than ocean depths, it is appropriate to use a cylindrical coordinate system for long range propagation. Customarily we define z as depth, r as range outward from the origin, and ϕ as the azimuthal angle ($0 \rightarrow 2\pi$) defining direction along a radial in the horizontal plane as depicted in Figure 3. In general, full 3-D modeling of the propagation is seldom done due to mathematical and computational complexity. It is often a good approximation to the real ocean acoustic environment to consider it azimuthally invariant, i.e., to assume that environmental parameters such as sound-speed profile, water depth, and bottom composition are independent of azimuthal angle to the source. With this assumption, we concentrate the analysis in depth versus range.

As mentioned in the introduction, the PE method is used in this thesis to model acoustic propagation. The parabolic equation method was introduced into underwater acoustics in the early 1970s by Hardin and Tappert (1973) who devised an efficient numerical solution scheme based on fast Fourier transforms. We will derive a PE solution in a 2-D constant-density fluid environment where we have assumed azimuthal symmetry and hence no dependence on the ϕ coordinate.

We begin with the wave equation for a constant-density medium in cylindrical coordinates (r,z) independent of ϕ

$$\nabla^2 p - \frac{1}{c^2}\frac{\partial^2 p}{\partial t^2} = 0 \; . \tag{1}$$

We now assume we have a steady state, time-harmonic acoustic field

$$p(r,z,\varpi t) = p(r,z)e^{-i\varpi t} \; . \tag{2}$$

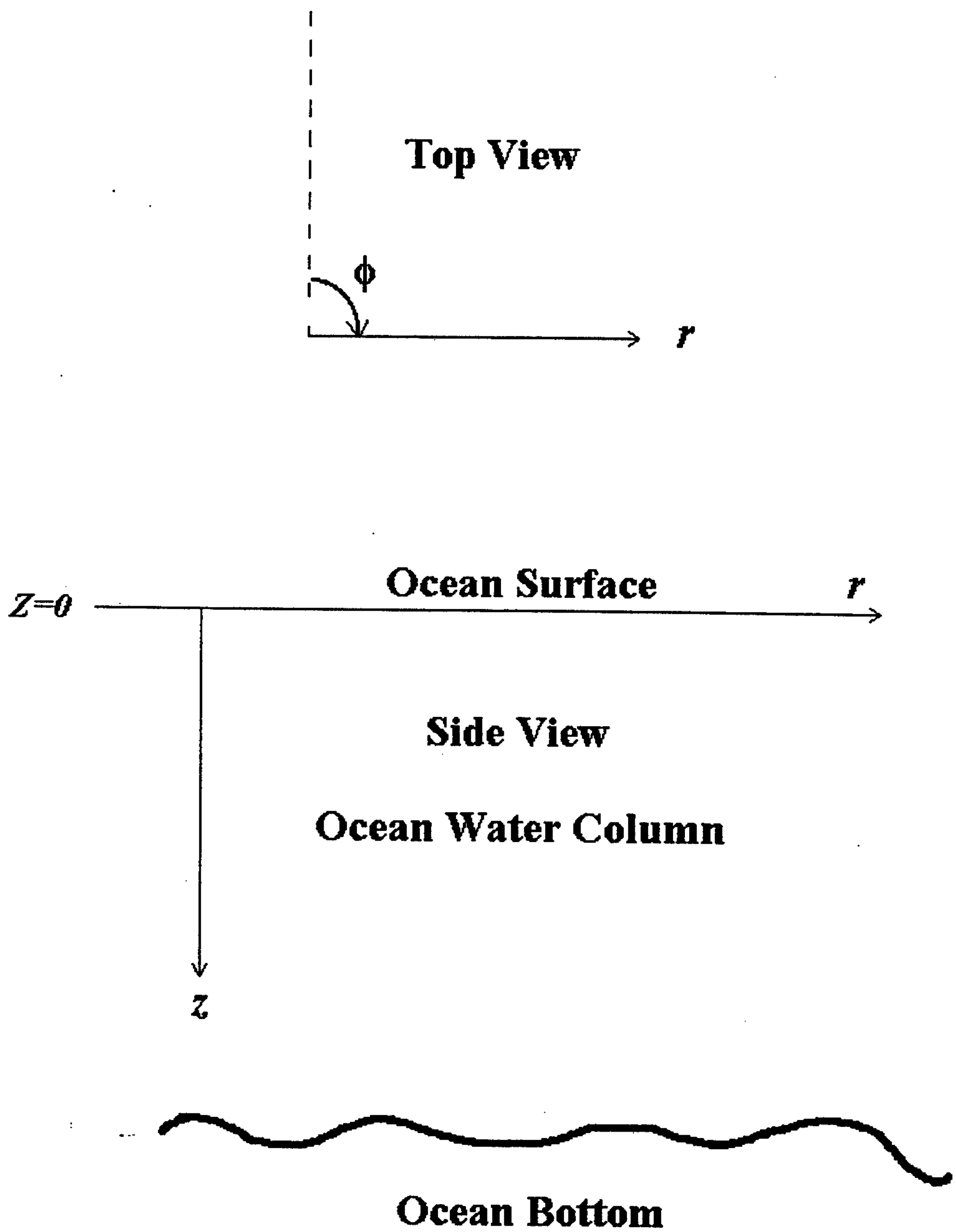

Figure 3. Cylindrical coordinates in ocean.

Substituting this into Eq. (1) leads to the Helmholtz equation,

$$\frac{\partial^2 p}{\partial r^2}+\frac{1}{r}\frac{\partial p}{\partial r}+\frac{\partial^2 p}{\partial z^2}+k_0^2 n^2 p=0 \ , \tag{3}$$

where $p(r,z)$ is the acoustic pressure, $k_0=\frac{\omega}{c_0}$ is the reference wave number, $n(r,z)=\frac{c_0}{c(r,z)}$ is the index of refraction, c_0 is the reference sound speed, and $c(r,z)$ is the acoustic sound speed. It is within $c(r,z)$ that all features of the environment are represented.

Tappert (1977) assumed the solution of Eq. (3) in terms of an outgoing Hankel function with an envelope function $\psi(r,z)$,

$$p(r,z)=\psi(r,z)H_0^{(1)}(k_0 r) \ , \tag{4}$$

where $\psi(r,z)$ is assumed to be slowly varying in range. In the far-field $(k_0 r >> 1)$, the Hankel function can be approximated by

$$H_0^{(1)}(k_0 r)\cong\sqrt{\frac{2}{\pi k_0 r}}e^{i\left(k_0 r-\frac{\pi}{4}\right)} \ , \tag{5}$$

thus an alternative relationship between the acoustic pressure, $p(r,z)$, and the slowly modulating envelope function, $\psi(r,z)$, is

$$p(r,z)=P_0\sqrt{\frac{R_0}{r}}\psi(r,z)e^{ik_0 r} \ . \tag{6}$$

This is the standard definition of the so-called "PE field function" ψ scaled such that at $r=R_0$, $|\psi|=1$ and $|p|=P_0$. Substituting (6) into (3) yields

$$\frac{\partial^2\psi}{\partial r^2}+2ik_0\frac{\partial\psi}{\partial r}+\frac{\partial^2\psi}{\partial z^2}+k_0^2\left(n^2-1\right)\psi=0 \ . \tag{7}$$

Now we introduce the crucial paraxial approximation based on the slowly modulating character of ψ,

$$\frac{\partial^2\psi}{\partial r^2}<<2ik_0\frac{\partial\psi}{\partial r} \tag{8}$$

We then obtain the following wave equation,

$$2ik_0\frac{\partial\psi}{\partial r}+\frac{\partial^2\psi}{\partial z^2}+k_0^2\left(n^2-1\right)\psi=0\ , \tag{9}$$

which is the standard parabolic equation. This can be rewritten as

$$\frac{\partial\psi}{\partial r}=\frac{ik_0}{2}\left(n^2-1+\frac{1}{k_0^2}\frac{\partial^2}{\partial z^2}\right)\psi\ , \tag{10}$$

which is the form first introduced to the underwater acoustics community by Tappert (1974).

Equation (10) is a one-way wave equation which can be solved by a range-marching numerical technique. The UMPE model applied in this thesis uses the split-step Fourier (SSF) method (Hardin and Tappert, 1973) which solves the parabolic equation by Fourier transform techniques. Define the complex Fourier transform pair as

$$\psi(r,z)=\int_{-\infty}^{\infty}\psi(r,k_z)e^{ik_z z}dk_z=F^{-1}\left[\psi(r,k_z)\right]\ , \tag{11}$$

$$\psi(r,k_z)=\frac{1}{2\pi}\int_{-\infty}^{\infty}\psi(r,z)e^{-ik_z z}dz=F\left[\psi(r,z)\right]\ , \tag{12}$$

where k_z is the vertical wave number. We may rewrite Eq. (10) as

$$\frac{\partial\psi}{\partial r}=ik_0\left(T_{op}+U_{op}\right)\psi\ , \tag{13}$$

where

$$T_{op}=\frac{1}{2k_0^2}\frac{\partial^2}{\partial z^2}\ , \tag{14}$$

represents the kinetic energy operator and

$$U_{op}=\frac{1}{2}\left(n^2-1\right)\ , \tag{15}$$

represents the potential energy operator. This representation of the operators as kinetic and potential energy operators is especially insightful when one wishes to form the ray equations which have Hamiltonian form (Smith, 1992).

In the PE/SSF method, solutions of ψ are marched out in range by

$$\psi(r+\Delta r) = e^{-ik_0\Delta r T_{op}} e^{-ik_0\Delta r U_{op}} \psi(r) \quad . \tag{16}$$

The operator U_{op} is simply a multiplication operator in z-space but T_{op} contains cross terms which couple different depths. However, T_{op} is a multiplication operator in vertical wave number space. It is therefore desirable to separate the application of each operator, one in z-space and one in k-space (here, k is the vertical wave number). In other words, the PE field function ψ is specified at some range r initially in the z-domain. A transformation is made to the k-domain followed by a multiplication of the k-space operator $e^{ik_0\Delta r \hat{T}_{op}}$ where $\hat{T}_{OP}$ is the corresponding kinetic energy operator in the wave number domain. The result is then transformed again to the z-domain and is followed by a multiplication of the z-space operator $e^{ik_0\Delta r U_{op}}$. The final result is the field function at $r+\Delta r$, that is,

$$\psi(r+\Delta r, z) = e^{-ik_0\Delta r U_{op}(r,z)} \times F^{-1}\left\{ e^{-ik_0\Delta r \hat{T}_{op}(r,k)} \times \left[F(\psi(r,z))\right]\right\} \quad . \tag{17}$$

This is the general algorithm of the PE/SSF method.

Previously, we have assumed the operators took the forms defined by Eq. (14) and (15). These forms are commonly referred to as the "standard PE" and are only one set of a number of various operator forms. In our simulation, we will use a higher order form which was introduced by Thomson and Chapman (1983) referred to as the "wide-angle" PE approximation (WAPE) with operators given by

$$\hat{T}_{WAPE}(k) = 1 - \left[1 - \left(\frac{k}{k_0}\right)^2\right]^{1/2} , \tag{18}$$

$$U_{WAPE}(z) = -\left[n(z) - 1\right] \quad . \tag{19}$$

We then need to define the initial conditions for the PE field function, $\psi(r=0,z)$. It is desirable to begin the calculation by specifying the source in the k-domain. Thomson and Bohun (1988) have shown that a wide angle source can be defined as

$$\psi(0,k) = \Delta k \frac{1}{2}\left(\frac{2R_0}{\pi k_0}\right)^{\frac{1}{2}}\left(1-\left(\frac{k}{K_0}\right)^2\right)^{-\frac{1}{4}}, \left(|k| < k_0\right), \tag{20}$$

where $k=k_0$ corresponds to a propagation angle of 90°.

B. TRAVEL TIME ANALYSIS

The calculation of the time domain arrival structure at a given range is an integral part of the analysis in this thesis. The pressure field in the time domain is represented by

$$p(r,z,t) = F^{-1}\left[p_\omega(r,z)\right] = \sum_\omega p_\omega(r,z)e^{i\omega t}, \tag{21}$$

where $p_\omega(r,z)$ is a single frequency component. The arrival time structure at some fixed range $r=R$ can be computed using the complex field $p_\omega(R,z)$ for many frequencies and then Fourier transforming to obtain $p(R,z,t)$, the set of complex pressure values in the time domain. To avoid large transform sizes, the UMPE model basebands the solutions and shifts the center frequency bin to zero. To reduce the effect of side-lobes, we apply a Hanning filter over the bandwidth before transforming to the time domain. Additionally, we neglect the phase factor $e^{ik_0R} = e^{i\omega\frac{R}{c_0}}$ by simply performing the Fourier analysis on the field function $\psi_\omega(R,z)$. Therefore, the time domain is heterodyned around the value $t_o = R/c_o$ and arrival times are computed as values of "reduced time" or $(t-t_o)$.

C. ROUGH BOTTOM INTERFACE

The ocean bottom roughness is assumed to be characterized by a 2-D power law spectrum at high wave numbers which can be written as

$$W_2\left(k >> \frac{1}{L_{corr}}\right) = \alpha k^{-\beta}, \tag{22}$$

where L_{corr} is the correlation length of the roughness and β is the spectral exponent. (Note that our use of wave number is now with respect to range scales of interface roughness.) To give the full spectrum a realistically smooth structure, we assume the spectral form

$$W_2(k) = \frac{\mu}{\left(1 + L_{corr}^2 k^2\right)^{\beta/2}} . \qquad \textbf{(23)}$$

The rms roughness represents the average amplitude of the undulated bottom interface variation and the correlation length can be thought of as a scale of self-similarity. The normalization factor μ is defined in terms of the rms roughness σ, i.e.,

$$2\pi \int_0^\infty W_2(k) k dk = \sigma^2 \qquad \textbf{(24)}$$

and therefore

$$\mu = \frac{1}{\pi}\left(\frac{\beta}{2} - 1\right)\sigma^2 L_{corr}^2 \qquad \textbf{(25)}$$

We only need the 1-D roughness spectrum along the slice in the two dimensional profiles (depth z and range r). Along the direction of range propagation in cylindrical coordinates, we have

$$W_1(k) = 2\int_k^\infty \frac{K}{\sqrt{K^2 - k^2}} W_2(K) dK , \qquad \textbf{(26)}$$

where K is the total horizontal wave number and k is the wave number along the propagation direction. Substituting Eq. (23) and Eq. (25) into Eq. (26), we obtain

$$W_1(k) = \gamma\sigma^2 L_{corr}\left(1 + L_{corr}^2 k^2\right)^{-\left(\frac{\beta-1}{2}\right)} , \qquad \textbf{(27)}$$

where

$$\gamma = \frac{2}{\pi}\left(\frac{\beta}{2} - 1\right)\int_0^\infty \frac{dt}{\left(1 + t^2\right)^{\beta/2}} = \frac{\left(\frac{\beta}{2} - 1\right)}{\pi} \frac{\Gamma\left(\frac{1}{2}\right)\Gamma\left(\frac{\beta - 1}{2}\right)}{\Gamma\left(\frac{\beta}{2}\right)} , \qquad \textbf{(28)}$$

and $\Gamma(x)$ is the gamma function.

To avoid the annoying gamma function, the UMPE model assumes the 1-D spectrum has the form

$$W_1'(k) = \left(1 + L_{corr}^2 k^2\right)^{-\left(\frac{\beta-1}{2}\right)} . \qquad \textbf{(29)}$$

The roughness realization is then simply rescaled by the desired value of σ to provide the appropriate rms value.

D. SEDIMENT COMPOSITION

Yamamoto (1995) summarizes the transformation between three-dimensional wave number spectra and the velocity variabilities which determine the ocean sediment properties. This transformation can be simplified for our 2-D case. The 2-D compressional wave velocity structure in the sediment may be written as

$$c(x,z) = c_0\left(1+\delta_c(x,z)\right) \tag{30}$$

where $c(x,z)$ is the velocity at a point (x,z), c_o is the average velocity at the seafloor and $\delta_c(x,z)$ is the relative variability. The relative variability is modeled as a zero-mean quasistationary random function, i.e.,

$$\langle \delta_c(x,z) \rangle = 0 \tag{31}$$

$$\langle \delta_c(x,z)\delta_c(x',y') \rangle = \int_{-\infty}^{\infty}\int_{-\infty}^{\infty} S(k_x,k_z)x\cos\{k_x(x-x')+k_z(z-z')\}dk_x dk_z \tag{32}$$

The 2-D power spectrum of the relative velocity variability is denoted by $S(k_x,k_z)$. By definition, the variance $\langle \delta_c^2 \rangle$ represents the total energy of the power spectrum.

$$\langle \delta_c^2 \rangle = \int_{-\infty}^{\infty}\int_{-\infty}^{\infty} S(k_x,k_z)dk_x dk_z \tag{33}$$

It is a plausible assumption that the vertical power spectrum may be given by a power-law form

$$S_z(k_z) = Bk_z^{-\beta} \tag{34}$$

where β is the spectral exponent and B is the spectral strength constant. The 2-D power spectrum given by Yamamoto is

$$S(k_x,k_z) = \frac{\partial\beta B}{4}\left(\alpha^2 k_x^2 + k_z^2\right)^{-(\beta+1)/2} \tag{35}$$

where α is the aspect ratio and $\beta/2$ must be an integer

To produce a random realization of sediment volume fluctuations, we assume the complex wave number spectrum has a random amplitude and phase, $Ae^{i\phi}$, for each wave number component. The random amplitude of each component of the power spectrum can then be obtained by $A^2 = -\ln(r)$ where r is an independent, uniformly distributed random variable in the interval (0,1). The random phase ϕ is another independent, uniformly distributed random variable in the interval (0,2π). To avoid infinite magnitudes at low wave numbers, the spectrum is high-pass filtered. The filtered spectrum is then Fourier transformed to obtain a realization of the sound speed variability. The entire field of sediment fluctuations is first computed on a fine grid and then interpolated to match the computational grid of the PE/SSF algorithm. The entire scheme can be described as follows:

- **Step 1.** Construct the 2-D wave number field $(k_r(n), k_z(m))$, according to

$$\Delta k_r = \frac{2\pi}{r_{\max}}, \qquad k_r(n) = (n-1)\Delta k_r \qquad n = 1,2,\ldots,N, \tag{36}$$

$$\Delta k_z = \frac{2\pi}{(z_{\max} - z_{bot})}, \qquad k_z(m) = (m-1)\Delta k_z \qquad m = 1,2,\ldots,M - M_{bot}, \tag{37}$$

where

$r_{\max}$ = maximum propagation range,
N = FFT size in range direction,
$z_{\max}$ = maximum compution depth,
z_{bot} = average bottom depth
M = FFT size in depth direction,
M_{bot} = index of average bottom interface.

- **Step 2.** Generate two random numbers series for the random phase and amplitude,

$$A(n,m) = \sqrt{-\ln(a_{n,m})}, \tag{38}$$

$$\phi(n,m) = 2\pi b_{n,m} \,. \tag{39}$$

where

a, b = uniform random number distribution $0 \rightarrow 1$.

- **Step 3.** Compute the random phase and amplitude for every mesh point in the 2-D realized wave number field, $S'(k_r(n)k_z(m))$, i.e.,

$$S'(k_r(n), k_z(m)) = S(k_r(n), k_z(m))A(n,m)e^{i\phi(n,m)} \,. \tag{40}$$

- **Step 4.** Add high-pass filter to normalize the exponent amplitude at low wave number

- **Step 5.** Compute 2-D FFT to yield relative velocity variability,

$$\delta_c(r,z) = 2D\,FFT\left[S'(k_r(n)k_z(m))\right].$$

The velocity structure of the sediment realization is then given by:

$$c(r,z) = c_0 + c_0 \times \mathrm{Re}(\delta_c(r,z)). \tag{41}$$

E. BEAMFORMING

In underwater acoustic propagation, much of the information about the environment and the relative source/receiver locations is contained in the vertical structure of the acoustic field. This is especially true in shallow water environments where the vertical structure can be defined in terms of a relatively small number of modes of the acoustic waveguide. Because these modes are generally dispersive, the ability to resolve the vertical structure of the time arrival at the receiver can lead to estimations of the corresponding source location.

Compared to the directivity of single sensors, a beamformer permits one to listen preferentially to wavefronts propagating from one direction over another. In this sense, a beamformer implements a spatial filter (see, for example, Defotta *et al.*, 1988, Ziomek, 1995). Consider a line array of equally spaced elements positioned along the y-axis in an infinite, homogeneous medium with an undetermined number of remote sources. Let the output of an element located at the origin of coordinates due to the *lth* source be $s_l(t)$.

Under the assumption of plane-wave propagation in the far-field, a source from direction θ_ℓ produces the following sensor outputs:

$$e_n(t) = s_\ell\left(t + \frac{nd\sin(\theta_\ell)}{c}\right) , \tag{42}$$

where n is the array element index, d is the spacing, θ_ℓ is the angle of arrival from the *lth* source, and c is the speed of propagation. Beamforming is accomplished by applying weights and time delays to the individual element signals, and then coherently summing them. The beamformer output when viewed in the direction θ_m is then

$$b_m(t) = \sum_{n=0}^{N-1} w_n s_\ell\left(t + \frac{nd(\sin(\theta_\ell) - \sin(\theta_m))}{c}\right) \tag{43}$$

where the w_n are weights applied to each element's signal.

The directional response characteristics of the beamformer can be derived by considering a complex, plane-wave cw signal propagating across the array,

$$s_\ell(t) = e^{i\omega_\ell t} . \tag{44}$$

The source produces the following sensor outputs due to the arrival angle

$$e_n(t) = e^{i\omega_\ell t} e^{ink_\ell d\sin(\theta_\ell)} , \tag{45}$$

where $k_\ell = \frac{2\pi}{\lambda_\ell} = \frac{\omega_\ell}{c}$ is the wave number of the *lth* source. The beamformer output is then

$$b_m(t) = e^{i\omega_\ell t}\sum_{n=0}^{N-1} w_n e^{ink_\ell d[\sin(\theta_\ell) - \sin(\theta_m)]} = W(\theta_\ell)e^{i\omega_\ell t} , \tag{46}$$

where

$$W(\theta_\ell) = \sum_{n=0}^{N-1} w_n e^{ink_\ell d[\sin(\theta_\ell) - \sin(\theta_m)]} , \tag{47}$$

represents the spatial Fourier transform of the array weights.

A two-dimensional FFT (spatial and temporal) can be used to implement the beamforming operation for an equally spaced line array. For example, consider a line array having $N=8$ equally spaced elements as depicted in Figure 4. The signals from each element are sampled simultaneously at rate f_s to obtain a multichannel time series $x_{n,m}$. M-point FFTs are taken along each channel to obtain the temporal frequency response, $X_n(j)$, where j is the frequency bin number, i.e.,

$$X_n(j) = \sum_{m=0}^{M-1} w_n x_{n,m} e^{-i\left(2\pi/M\right)mj} \qquad , 0 \le j \le M-1 \ . \tag{48}$$

The $X_n(j)$ are represented in the figure as N horizontal rows of M FFT bins.

Next, the N cross-channel FFT is performed with appropriate weighting along the array, i.e.,

$$X(j,k) = \sum_{n=0}^{N-1} w_n X_n(j) e^{-i\left(2\pi/N\right)nk} \qquad , 0 \le k \le N-1 \tag{49}$$

The result of the N cross-channel FFT series to spatial frequency (or wave number) provides the phase difference information in depth for specific temporal frequencies. The relationships between the various indices and the variables used in the beamformer output are

$$f_\ell = \frac{j}{M} f_s \ , \tag{50}$$

$$k_l = \frac{k}{N} \frac{2\pi}{d} \ , \tag{51}$$

$$\theta_m = \sin^{-1}\left(\frac{c}{2\pi}\frac{k_\ell}{f_\ell}\right) \ , \tag{52}$$

where j and k are the indices in the frequency and wave number domains, respectively. In practice, θ_m is determined by interpolating between values of k_l. After the data has been interpolated to arrival angle/frequency space, an inverse FFT is taken along each angle bin to provide arrival angle as a function of travel time.

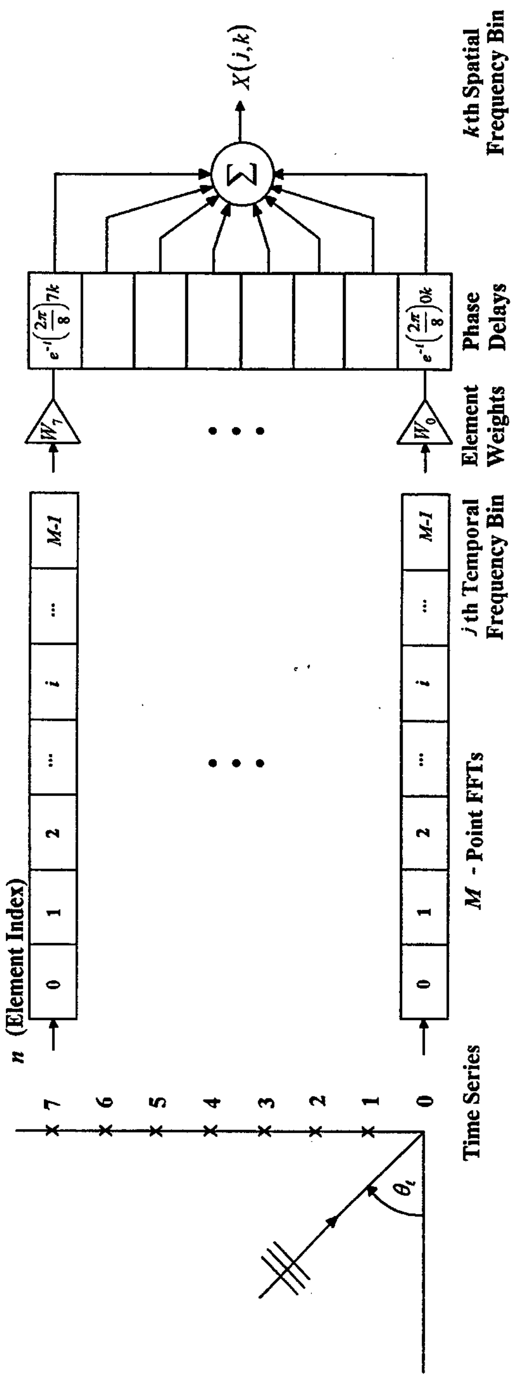

Figure 4. Beamforming example.
From [DeFotta, 1988]

III. MODEL SIMULATIONS

As was described in the introduction, the principal characteristic of most shallow-water propagation is dominated by bottom-interacting paths. Sound transmission in shallow water has an optimum frequency of propagation at longer ranges as shown by Jensen and Kuperman (1983). Optimum frequency is a general feature of ducted propagation in the ocean. It occurs as a result of competing propagation and attenuation mechanisms at high and low frequencies. In the high-frequency regime there is increasing volume and scattering loss with increasing frequency. At lower frequencies the situation is more complicated. With increasing wavelength the efficiency of the waveguide to confine sound decreases (the cutoff phenomenon). Hence propagation and attenuation mechanisms outside the waveguide (in the seabed) become important. In fact, the increased penetration of sound into a lossy seabed with decreasing frequency causes the overall attenuation of waterborne sound to increase with decreasing frequency. Thus we get high attenuation at both high and low frequencies, while intermediate frequencies have the lowest attenuation. As Jensen's study shows, the optimum frequency is in the range 200-800 Hz for a water depth of 200 m and we will use 200 Hz as our center frequency

We assume that the ocean bottom sediment is a fluid-like half-space which means that it supports only one type of sound wave, i.e., compressional waves. The information required for model simulations should include the following depth-dependent material properties: the sound speed profile in the water column and compressional wave speed, attenuation and the density in the seabed. For all cases, we will assume the water column is homogeneous with a constant sound speed.

This chapter presents the model simulation results of four test cases. Case 1 examines the propagation of a broadband, impulsive source over a flat, homogeneous bottom. Case 2 examines the propagation in a similar environment with a rough bottom interface. We then examine which parameters, i.e., rms roughness, correlation length or ratio of them, dominates the beam resolution. Case 3 is also similar to Case 1 but with realistic bottom volume fluctuations. The factors which most strongly influence resolution in Case 2 and Case 3 will be combined into Case 4.

The basic range-independent parameters used in the UMPE model are listed in Table 1.

Model Type	Wide Angle PE
Source Function Type	Wide Angle Source
Reference Sound Speed	1500.00 m/s
Bottom Depth	200.0 m
Maximum Computational Depth	400.0 m
Mesh Points For Positive Depths	512
Maximum Range	10.0 km
Step In Range	2.0 m
Mesh Points In Range	5000
Source Depth	100.0 m
Center Frequency	200.0 Hz
Frequency Bandwidth	100.0 Hz
Number Of Frequencies	256
Sound Speed In Water	1500 m/s
Sound Speed In Sediment	1600 m/s
Density In Sediment	1500 kg/m^3
Attenuation In Sediment	0.2 dB/m/kHz

Table 1. UMPE Model Parameters

A. CASE 1: RANGE INDEPENDENT

We begin with the simple case consisting of a constant speed water column and fluid-like homogeneous sediment separated by a flat interface. The corresponding transmission loss field for the center frequency is depicted in Figure 5. We note the symmetric constructive interference due to the finite number of trapped, propagating normal modes. By Snell's law, there is a critical angle at $\arccos\frac{1500}{1600}$ =20.4° (relative to horizontal) below which no energy is transmitted into the bottom. From the UMPE output field with beamforming at 10,000 m, we obtain the angle-time plot shown in Figure 6. As expected, this energy arrives primarily near horizontal with an aperture of approximately ±20°. The steeper-angle energy ≥20° is rapidly lost by transmission into the seabed. Furthermore, the lowest modes arrive first, before the higher modes, as would be expected

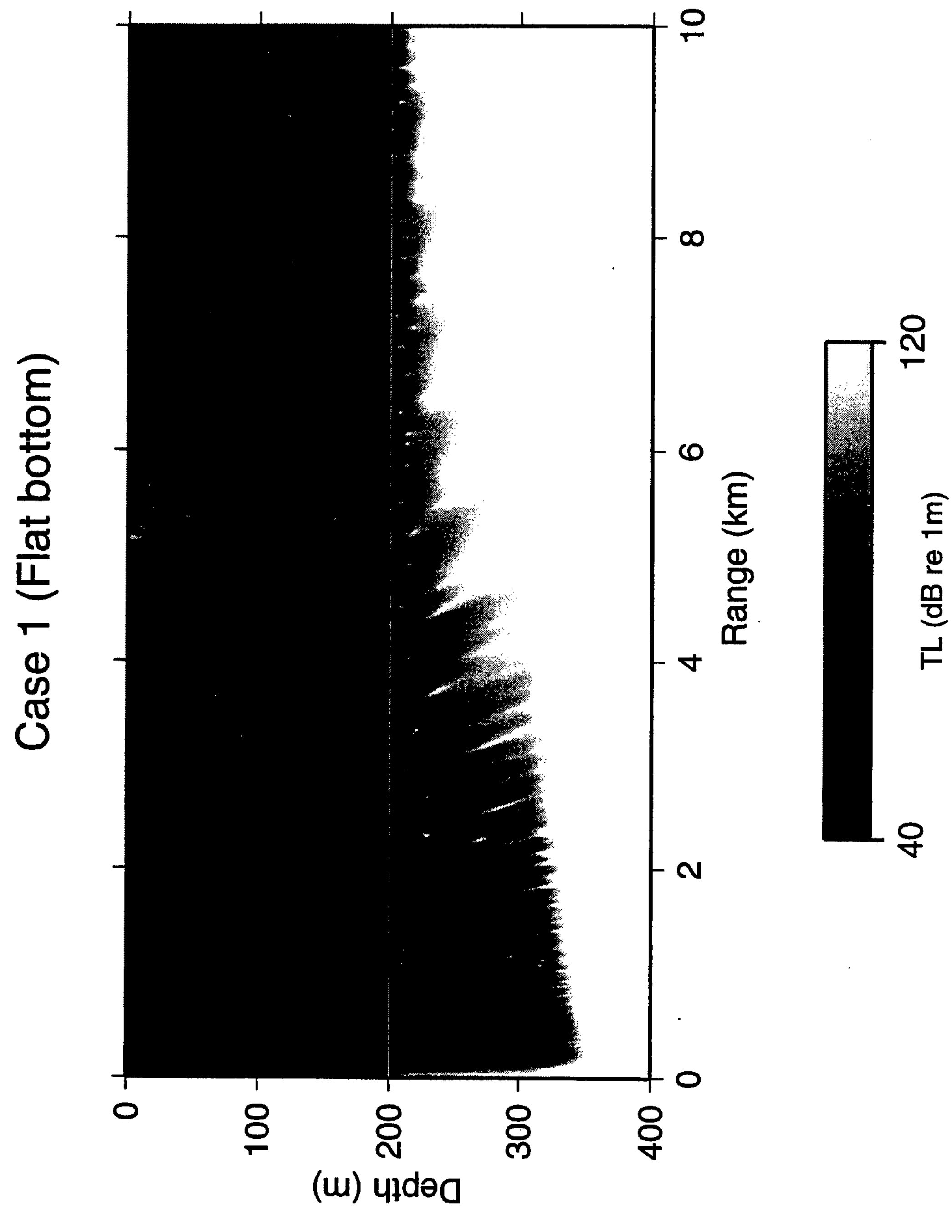

Figure 5. Range-depth transmission loss field for flat bottom interface.

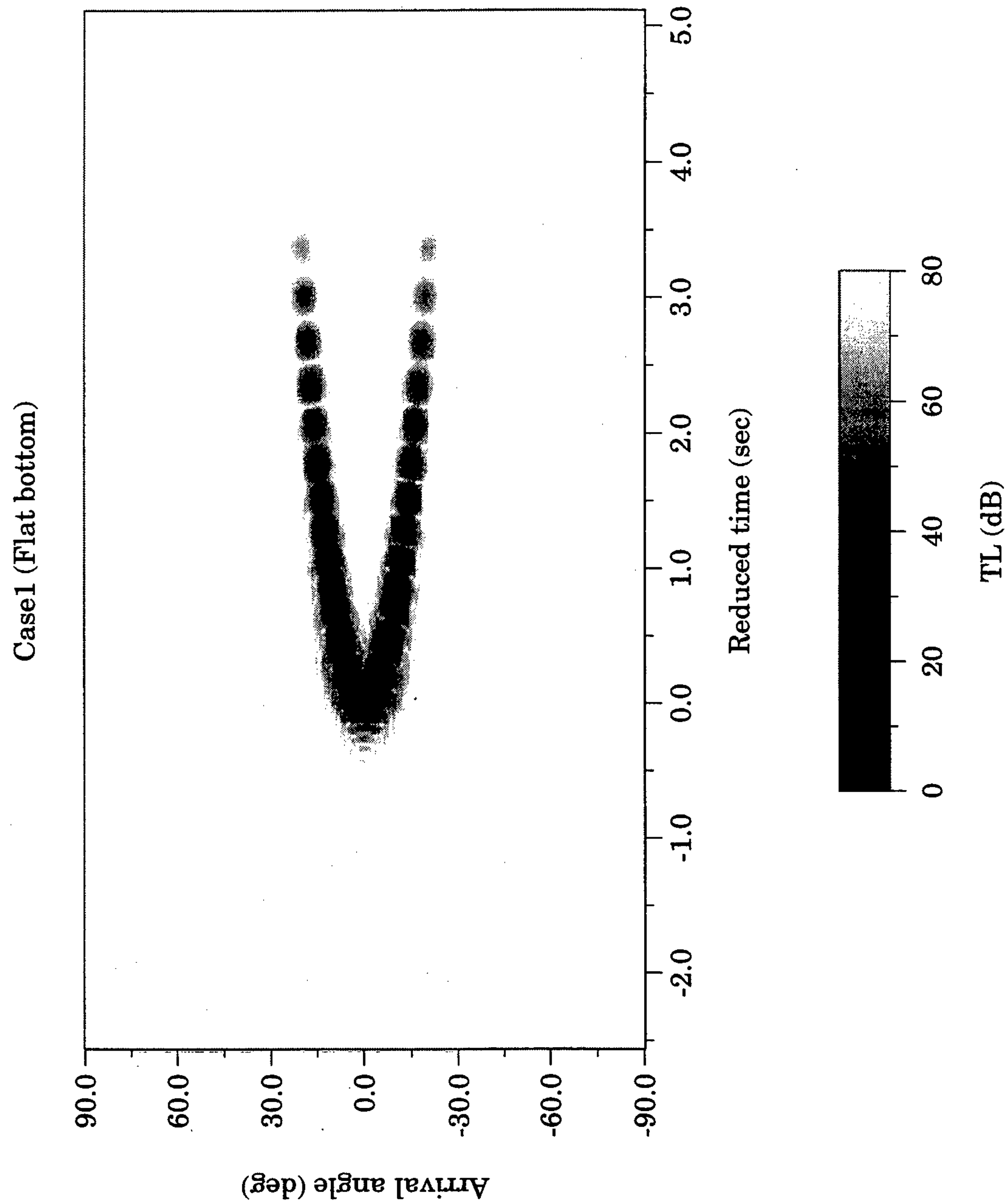

Figure 6. Arrival angle-time plot for flat bottom interface.

from an analysis of the modal dispersion in this environment. A standard calculation of the number of trapped modes was found to be consistent with the number of arriving modal peaks when the range of the transmission loss palette was extended to expose the weakest modal arrivals.

B. CASE 2: ROUGH BOTTOM INTERFACE

A rough seafloor will cause attenuation of the mean acoustic field propagating in the ocean waveguide due to incoherent scattering thereby decreasing the mean signal to noise ratio. For individual pulse transmissions, the instantaneous signal becomes smeared in time and space due to mode coupling. A rough bottom interface is added to the environment of Case 1 in order to investigate the effect of scattering on the instantaneous resolution of the pulse in the water column.

As described in Chapter II, there are two parameters that control the roughness, i.e., the rms roughness and the correlation length. In order to determine the dominant factor, we simulated two sets of comparisons. In one, the correlation length is fixed at 1000 m and the rms roughness has values of 2, 5, and 10 m. In the other, the rms roughness is fixed at 2 m with correlation lengths of 40, 200, and 400 m. Figure 7-12 show the beamformed angle-time plots at 10,000 m. We can see that increasing the rms roughness and decreasing the correlation length will reduce the resolution but it is difficult to see which factor dominates. However, the distortion changes look similar and suggest that the ratio of rms roughness and correlation length may be the important parameter. We simulated several realizations with fixed ratio of the rms roughness and the correlation length to confirm our hypothesis, specifically, (rms roughness): (correlation) = 1:500, 1:100 and 1:20. The beamformed results are displayed in Figure 13-15. Combined with the previous simulations, we find that higher ratios retain higher resolution and lower ratios degrade the resolution more severely. Figure 16-18 show single frequency (200 Hz) transmission loss fields in depth-range slices for various rough interface realizations. Compared to the flat bottom case, we see that there is more energy penetration into the

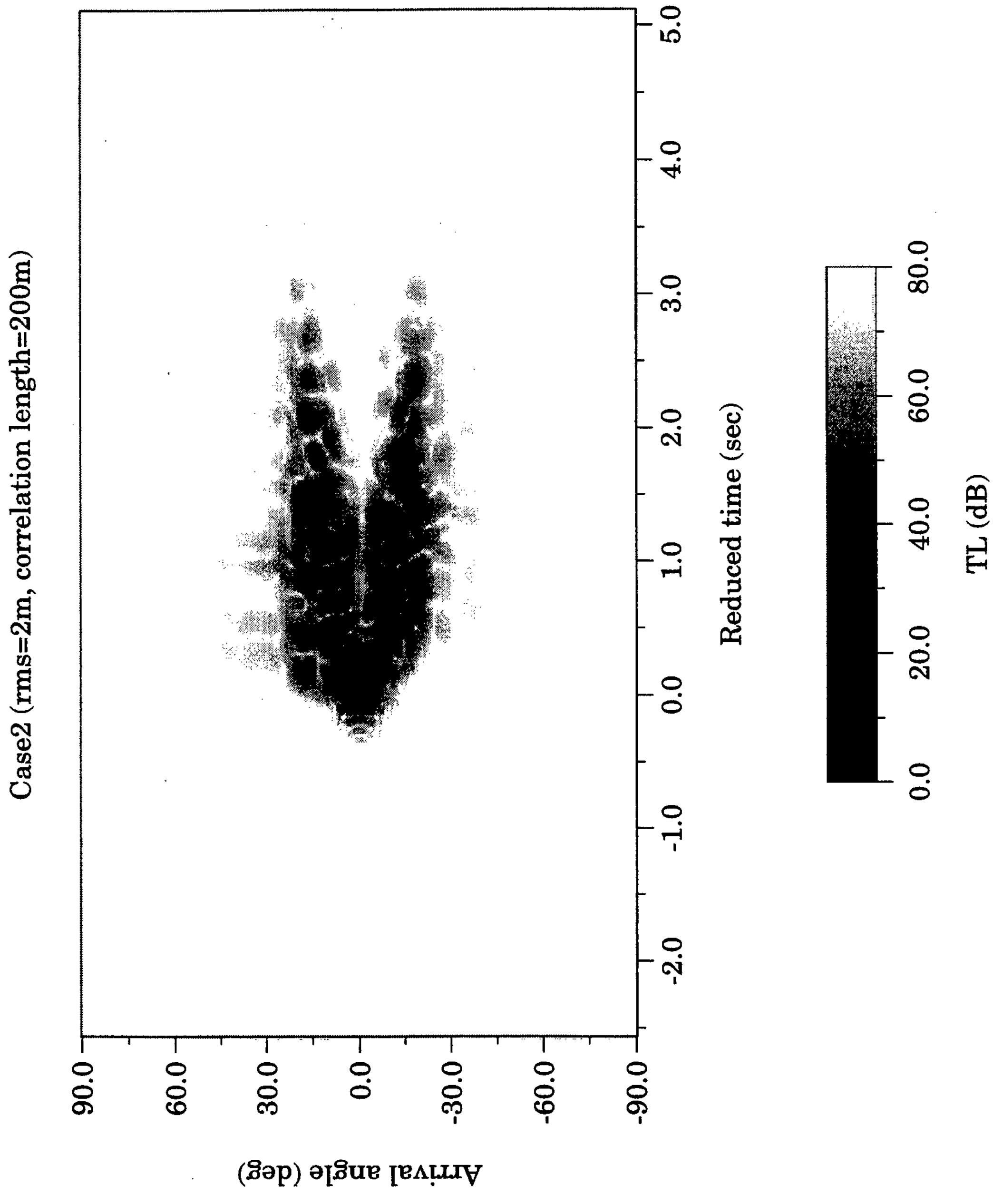

Figure 7. Arrival angle-time plot for rough bottom interface with rms roughness = 2m and correlation length = 1,000m.

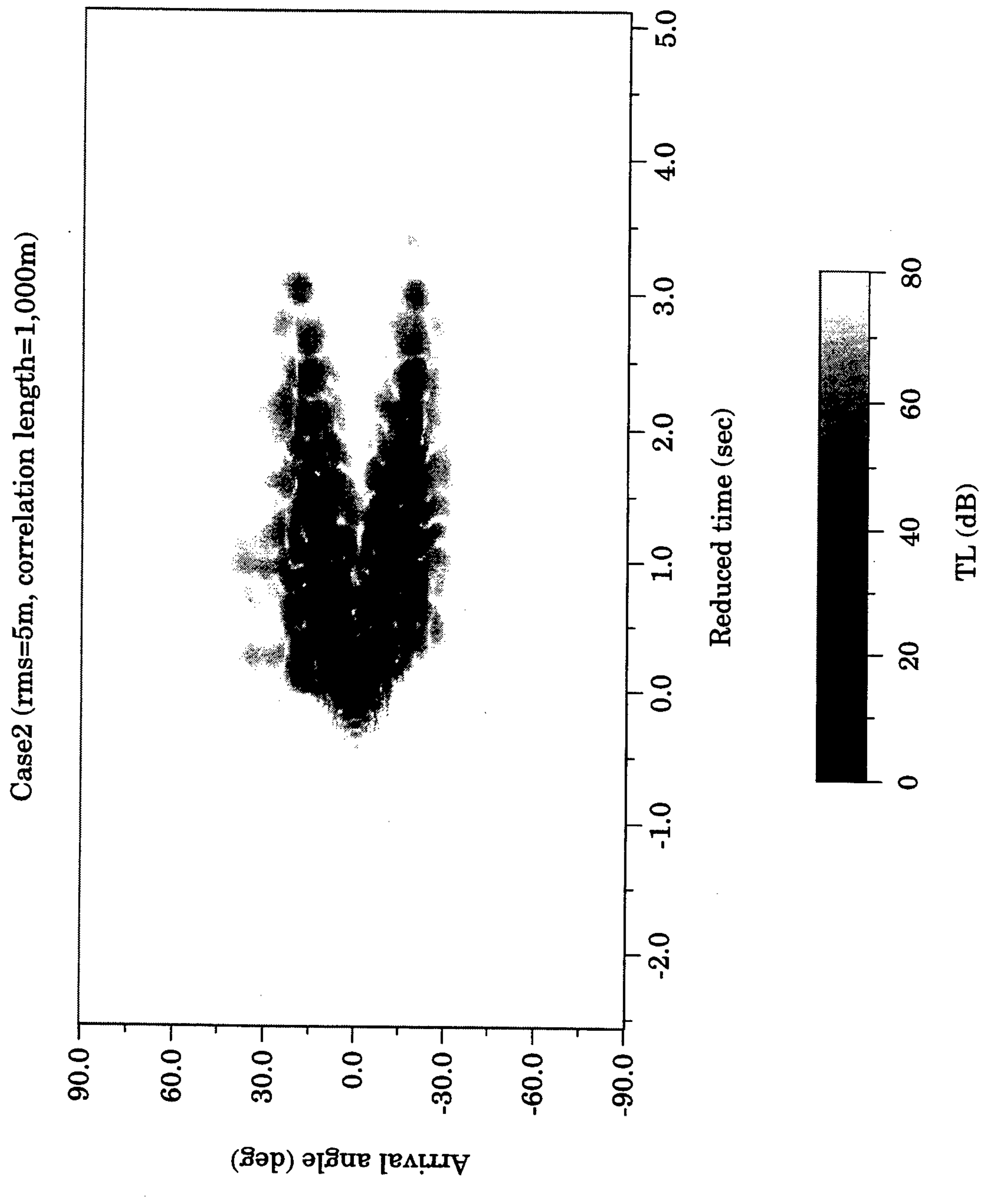

Figure 8. Arrival angle-time plot for rough bottom interface with rms roughness = 5m and correlation length = 1,000m.

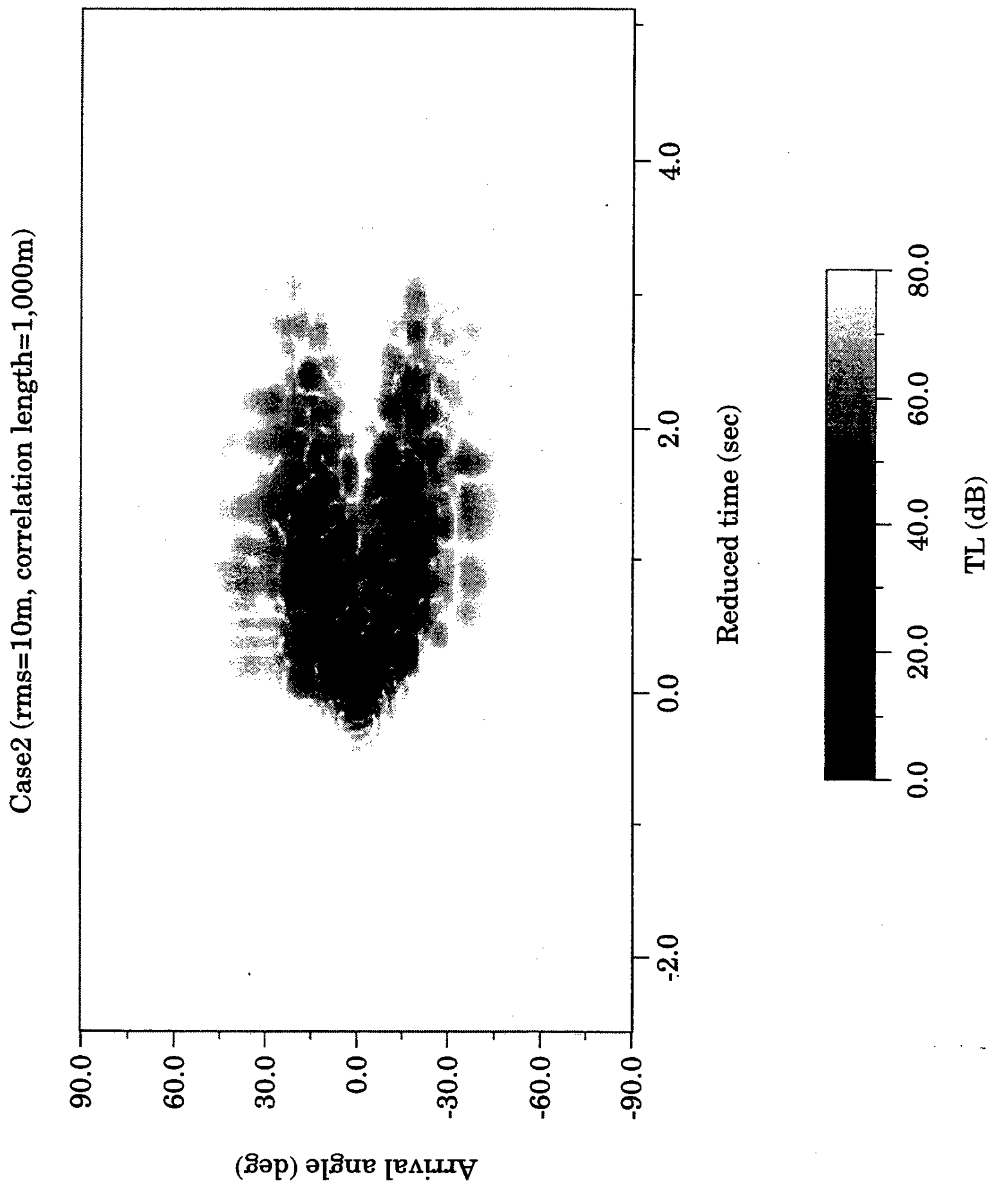

Figure 9. Arrival angle-time plot for rough bottom interface with rms roughness = 10m and correlation length = 1,000m.

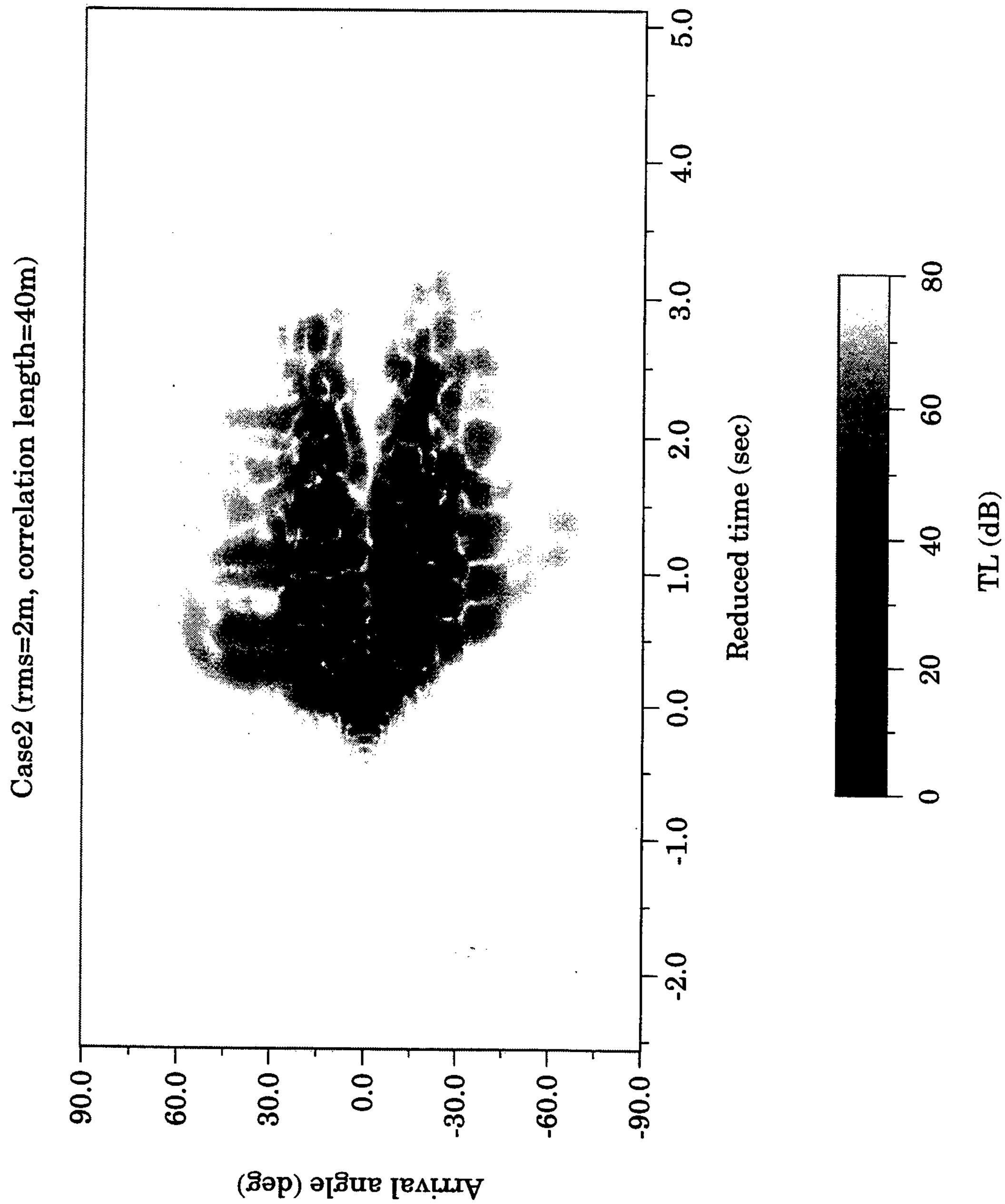

Figure 10. Arrival angle-time plot for rough bottom interface with rms roughness = 2m and correlation length = 40m.

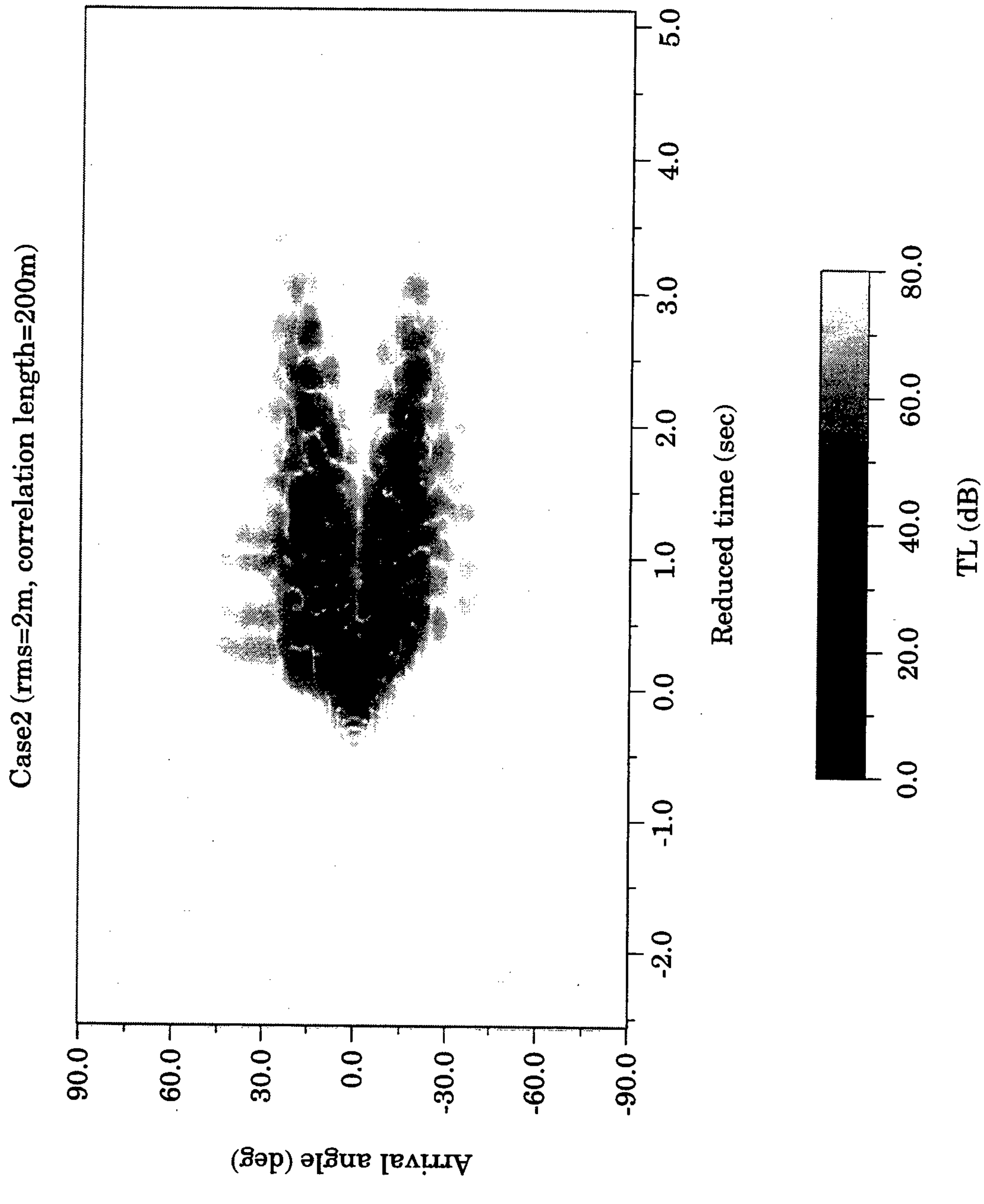

Figure 11. Arrival angle-time plot for rough bottom interface with rms roughness = 2m and correlation length = 200m.

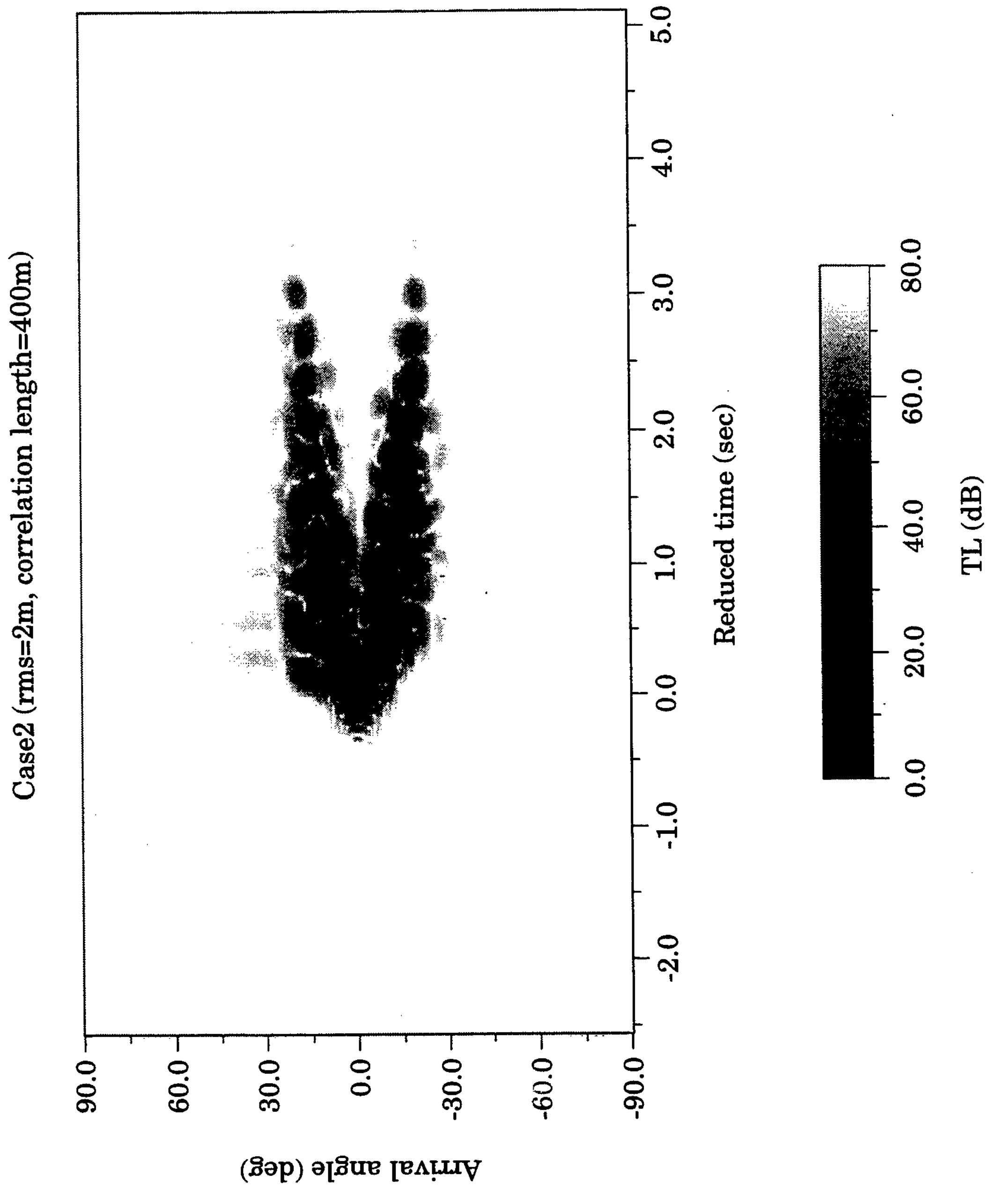

Figure 12. Arrival angle-time plot for rough bottom interface with rms roughness = 2m and correlation length = 400m.

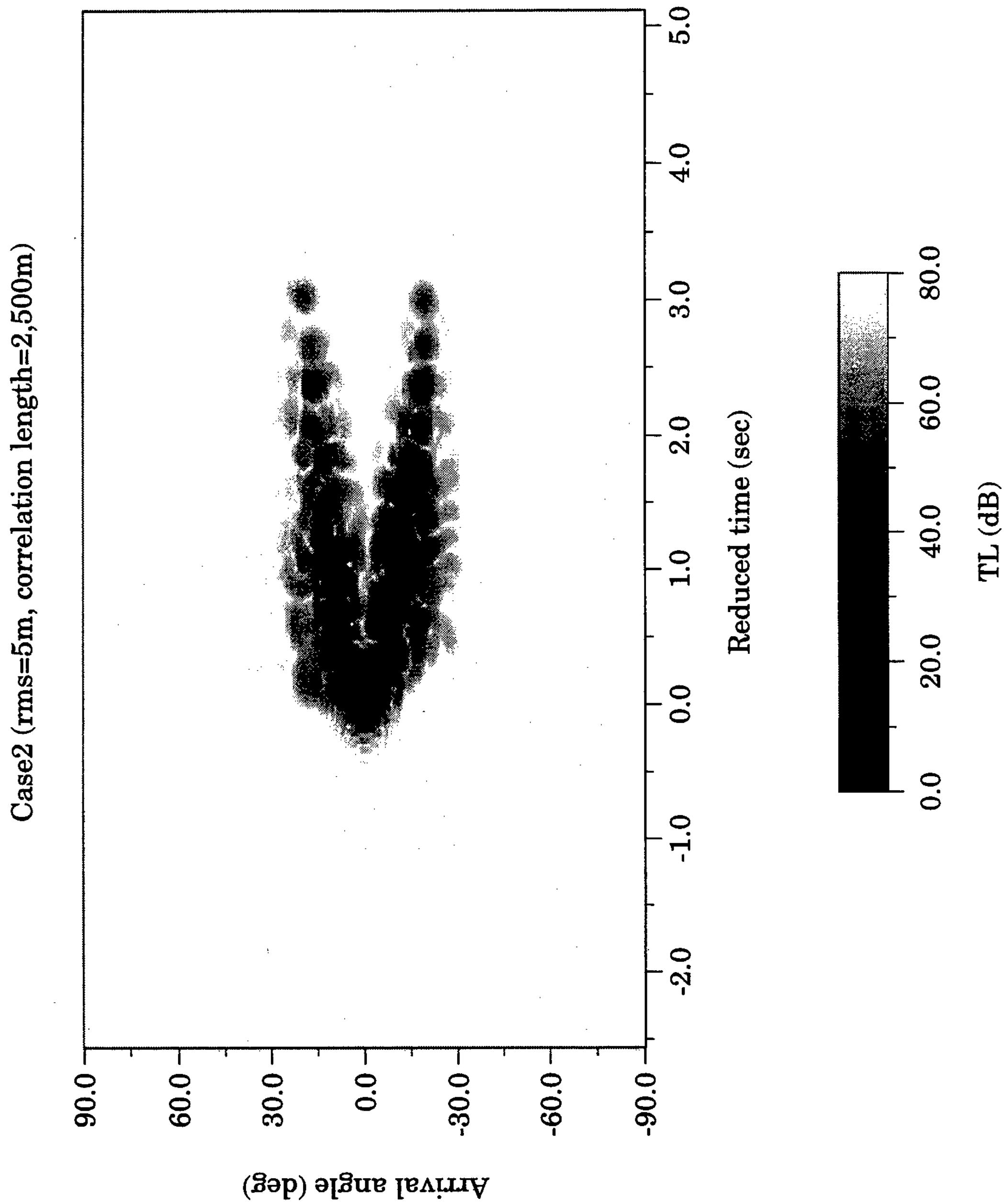

Figure 13. Arrival angle-time plot for rough bottom interface with rms roughness = 5m and correlation length = 2,500m.

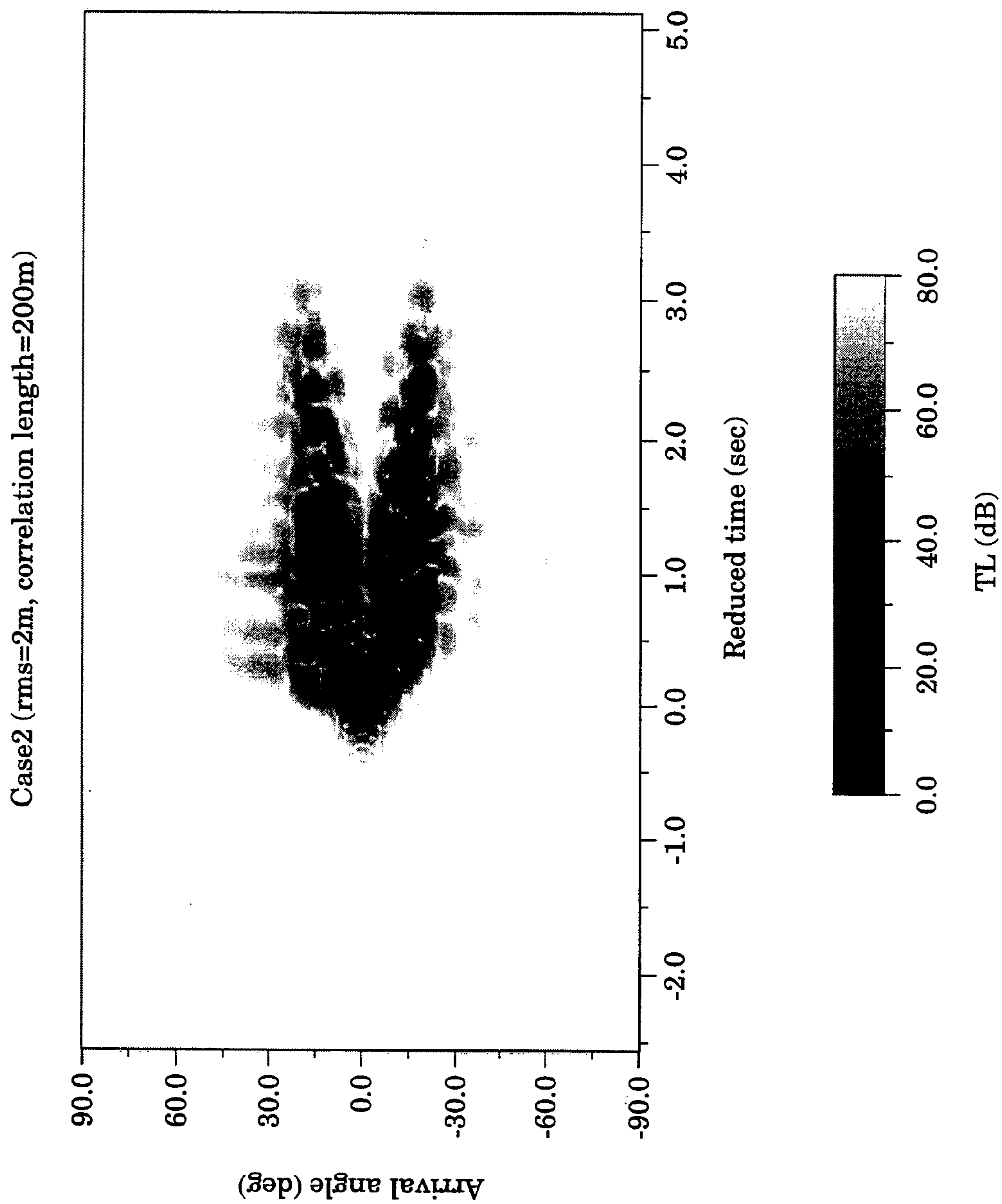

Figure 14. Arrival angle-time plot for rough bottom interface with rms roughness = 2m and correlation length = 200m.

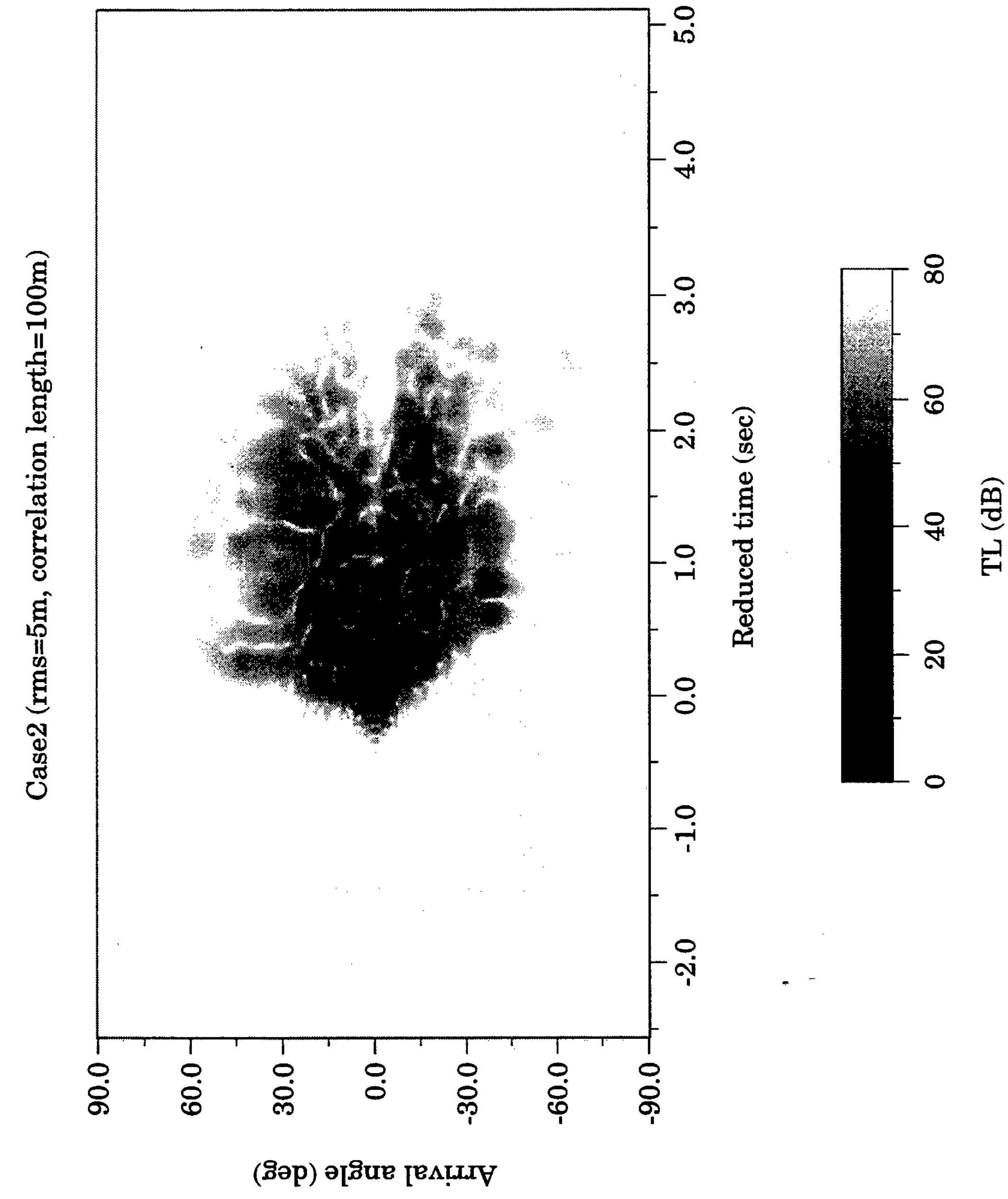

Figure 15. Arrival angle-time plot for rough bottom interface with rms roughness = 5m and correlation length = 100m.

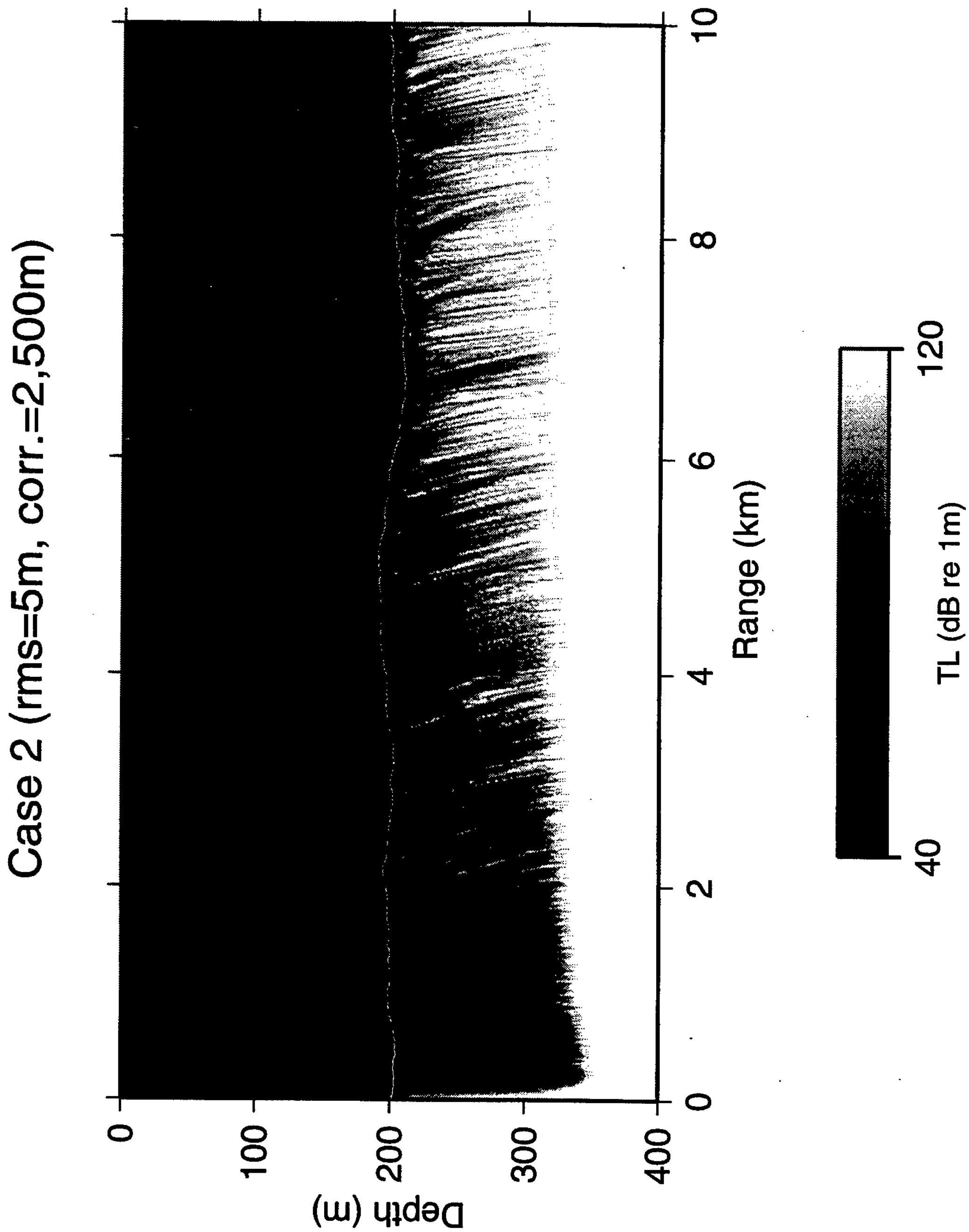

Figure 16. Range-depth transmission loss field for rough bottom interface with rms roughness = 5m and correlation length = 2,500m.

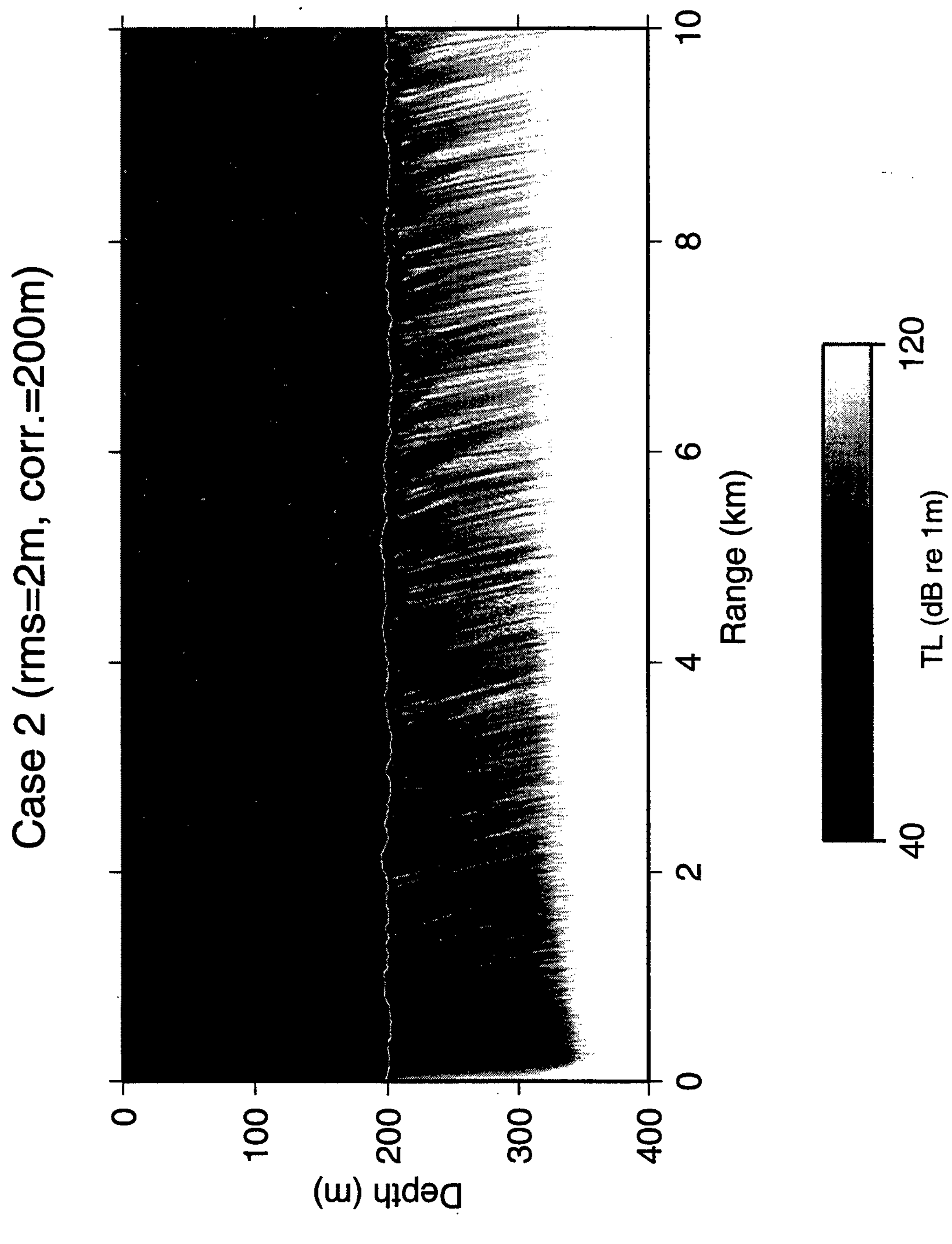

Figure 17. Range-depth transmission loss field for rough bottom interface with rms roughness = 2m and correlation length = 200m.

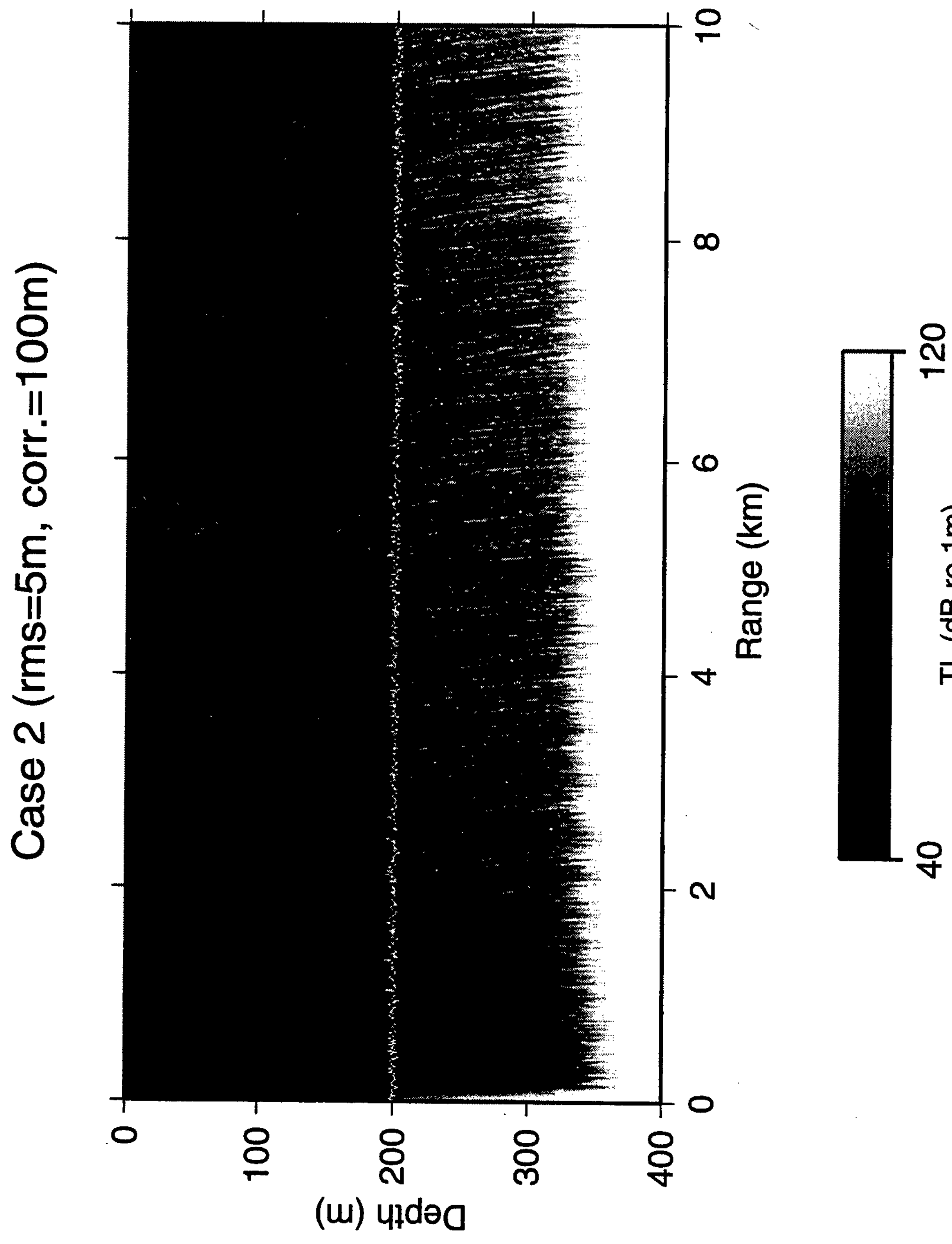

Figure 18. Range-depth transmission loss field for rough bottom interface with rms roughness = 5m and correlation length = 100m.

bottom at longer ranges, and the stable interference structure has broken down into a complex pattern.

C. CASE 3: SEDIMENT VOLUME FLUCTUATIONS

The scattering due to the velocity variability within the sediment is considered to be the major scattering mechanism in many geological fields in shallow water based on extensive measurements of acoustic backscattering and sediment cores (Jackson and Briggs 1992, Yamamoto 1995). The geology of shallow-water seabeds is complicated because of the physical, chemical, and biological activities which took place though the long geological time spans. The measurements of the velocity and density variabilities in the ocean are beyond this thesis subject. For our simulations, we shall use the sediment model described in Chapter II with some typical values extracted from Yamamoto's work.

In this case, we use a flat bottom interface and add the sediment volume perturbation. According to Yamamoto's model, the bottom sediment perturbation is controlled by three parameters: spectral exponent β, aspect ratio α, and the spectral strength constant B. In his conclusions, the spectral exponent β and aspect ratio α are fairly constant regardless of the sediment type but the spectral strength constant B varies depending on the sediment type and location. We will fix α and β and vary the values of B by choosing three typical spectral strength constants, e.g., 2×10^{-3}, 2×10^{-4} and 2×10^{-5} (units of B are $m^{1-\beta}$). The sediment field for strength constant $B = 2\times10^{-3}\ m^{1-\beta}$ is depicted in Figure 19. The rms value of the sound speed fluctuations in the sediment for this value of B is 22.4 m/s. The beamformed results for the three values of B are shown in Figure 20-22. The pulse shape does appear to degrade slightly as the spectral strength constant is increased. Overall, however, the sediment volume perturbation doesn't seem to affect the pulse resolution significantly.

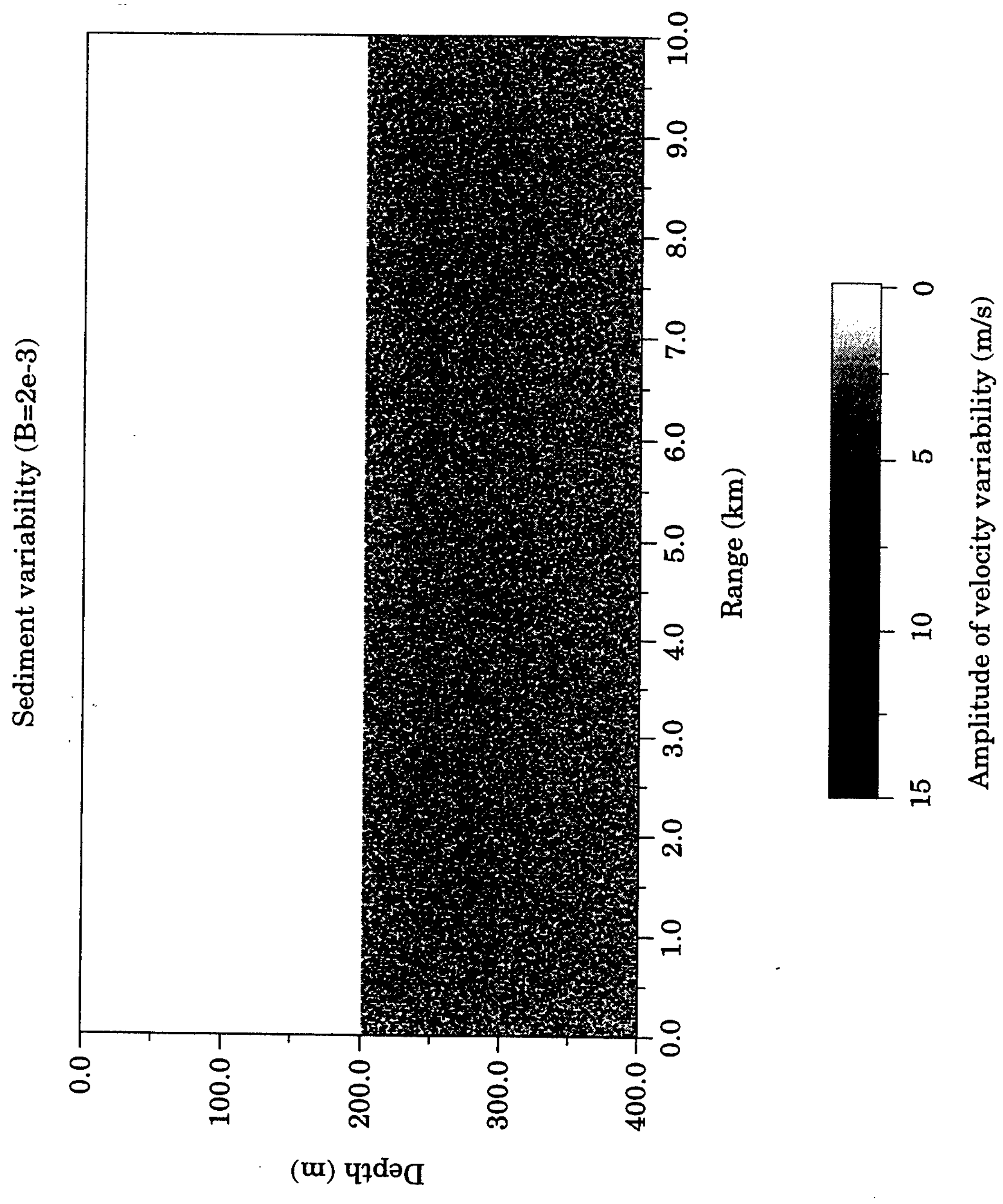

Figure 19. Sediment field for strength constant $B=2x10^{-3}$ $m^{1-\beta}$.

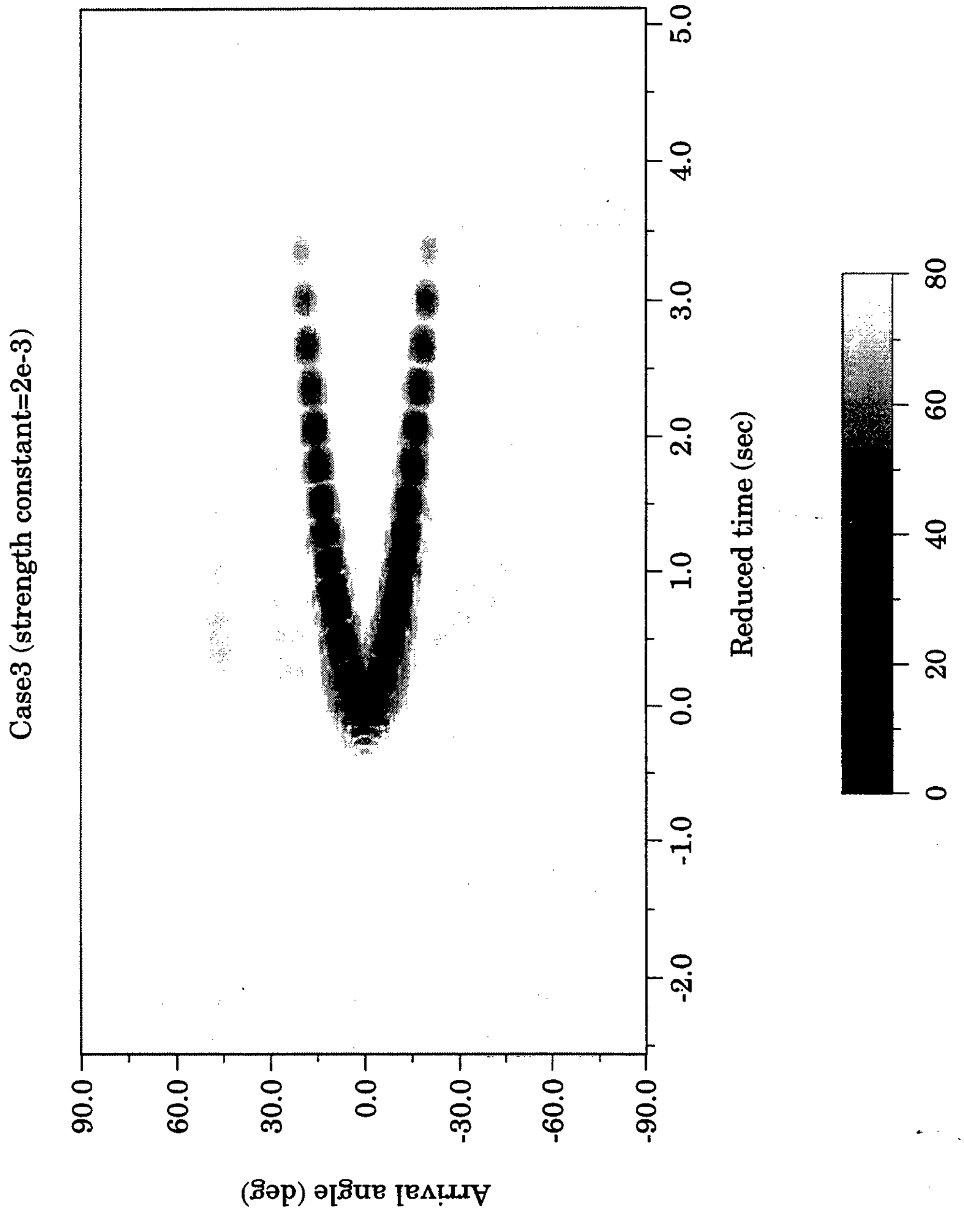

Figure 20. Arrival angle-time plot for sediment volume fluctuation with strength constant $B=2x10^{-3}$ $m^{1-\beta}$.

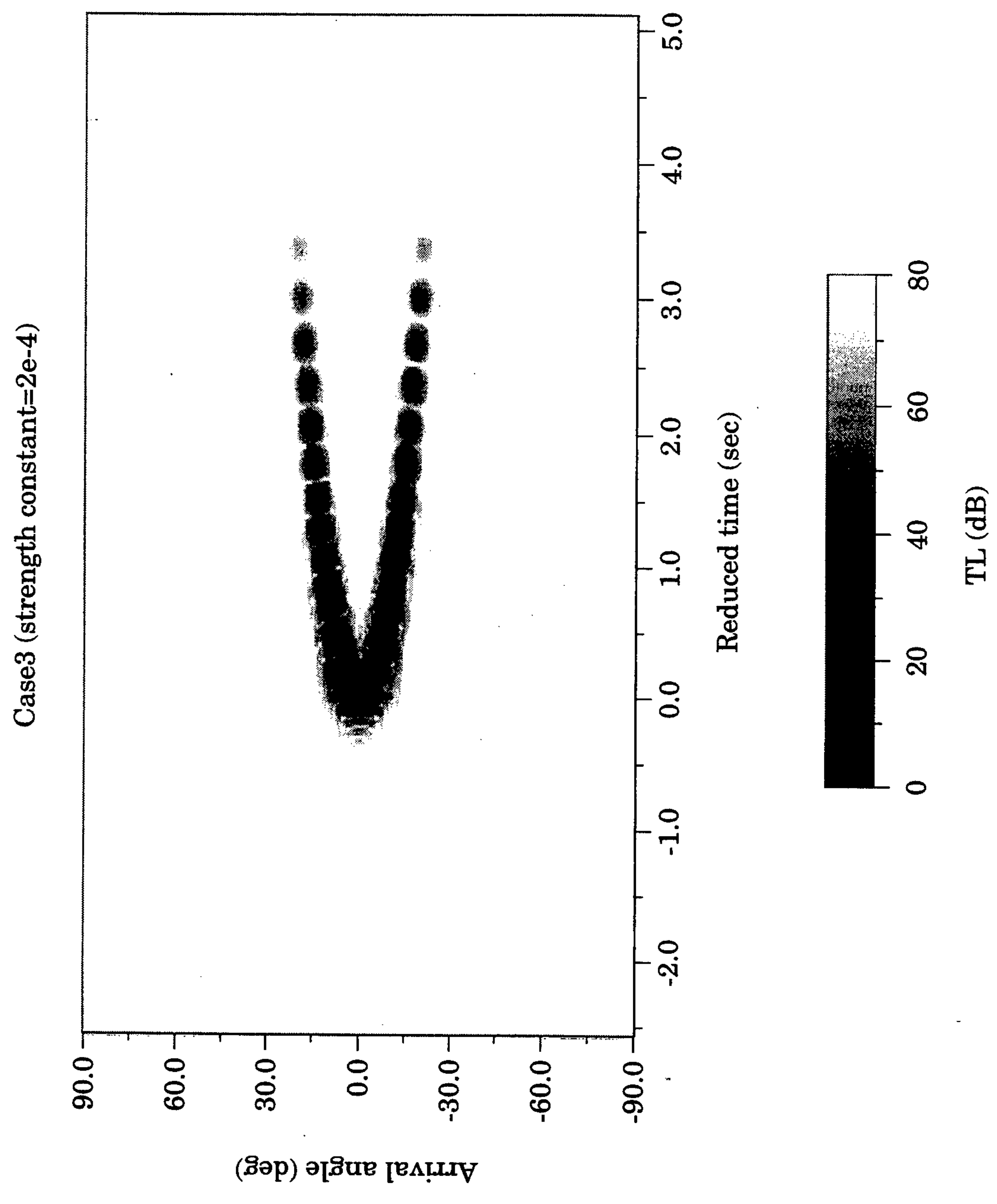

Figure 21. Arrival angle-time plot for sediment volume fluctuation with strength constant $B=2x10^{-4}\ m^{1-\beta}$.

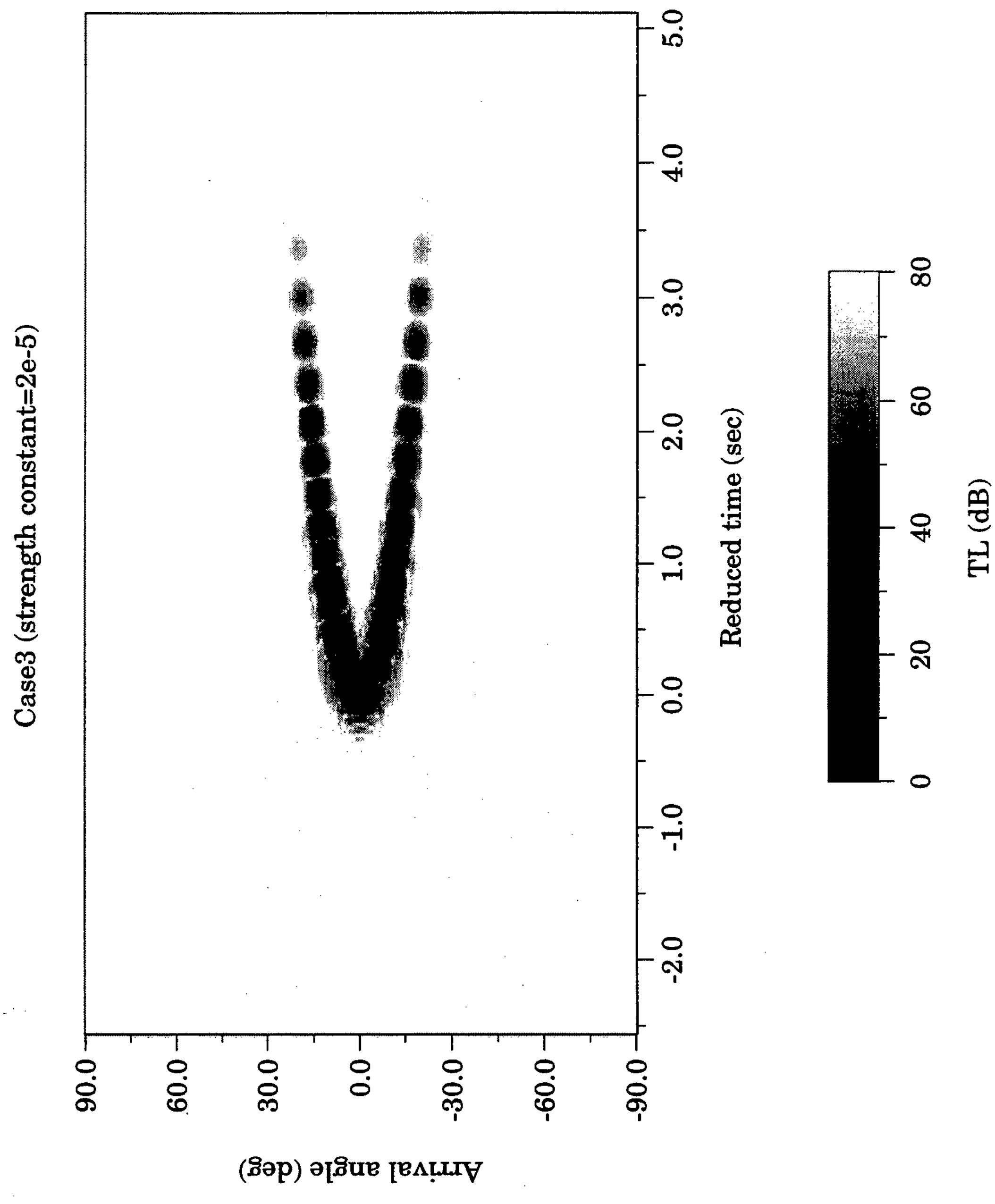

Figure 22. Arrival angle-time plot for sediment volume fluctuation with strength constant B=2x10^{-5} m$^{1-\beta}$.

D. CASE 4: ROUGH BOTTOM INTERFACE WITH SEDIMENT VOLUME FLUCTUATIONS

We have seen the effect of rough bottom interfaces and sediment volume fluctuations separately. We now need to combine these two factors. From Case 2 and Case 3 results, it appears that the effect of a rough bottom interface dominates the pulseresolution. The strongest sediment volume perturbation strength constant, $B = 2\times10^{-3}$ $m^{1-\beta}$, was chosen to produce the largest volume effect. The interface correlation length was fixed at 1000 m and the rms roughness was varied from 2 m to 10 m. Comparing these results to those cases with no volume fluctuations showed little difference indicating that these levels of interface roughness dominate the effects on pulse resolution.

E. PULSE RESOLUTION ANALYSIS

We have shown that the effect of the bottom roughness and sediment volume fluctuation degrades low frequency pulse resolution in shallow water propagation. In this section, we will quantify the effect of rough bottom and sediment volume fluctuation on pulse resolution in order to obtain a clearer relationship. The conventional angle resolution is defined as an angle width of $1/e$ peak amplitude. In order to simplify the Case 2 analysis, we fixed the correlation length at a value of 1000 m and varied the rms roughness. Figure 23 shows several slices in reduced times of 1, 1.5, 2, 2.5 and 3 seconds from an arrival angle-time plot for rms roughness of 0 (the Case 1 results), 2, 5, 10 and 20 m. Each reduced time data point is actually an average of five points spread over a time bin width of 0.2 sec, i.e., the datum for the reduced time of 1 sec is an average of data at 0.90, 0.95, 1.00, 1.05, and 1.10 sec. Polynomial fits to the data produce the smooth curves shown in the figures. We can see a good angle resolution at lower rms roughness values. As the rms roughness is increased, the resolution is found to degrade, particularly for the later arrival times This is expected since later arrivals correspond to higher modes which interact more strongly with the bottom. As an estimation of this effect, we note that the angular pulse width appears to double for an rms value of ~10 m corresponding to an rms: correlation ratio of 1:100.

In Figure 24. slices are taken at arrival angles 0, 5, 10, and 20 deg In this case, three points over a width of 1 deg are averaged to produce each data point shown. There is an anomalous point at an rms of 2 m due to unresolved peaks of two modes. This point was not used in the curve fit. The time resolution degrades when the rms roughness increases for all arrival angles except 0 deg. This is due to less bottom interactions of the horizontal propagation. Furthermore, we notice that the time width does not degrade as rapidly as the angular width. None of the rms roughness values appear to double the pulse width in time. The peak minimum transmission loss also increases with rms roughness as shown in Figure 25 by roughly 5 - 10 dB at an rms value of 10 m.

To perform a similar analysis of the Case 3 environment, the spectral exponent and aspect ratio were fixed. Obviously, the sediment volume fluctuations show more stable results with varying strength constant as depicted in Figure 26-28. The angle and time resolution change little with increasing strength constant. The peak (minimum) transmission loss also remains stable.

In Figure 29, the peak minimum transmission loss computed with the combined effects of a rough bottom interface and sediment volume fluctuations shows very similar results as in Figure 25. It is reasonable to conclude that these levels of bottom roughness dominate pulse resolution effects in simple shallow water propagation.

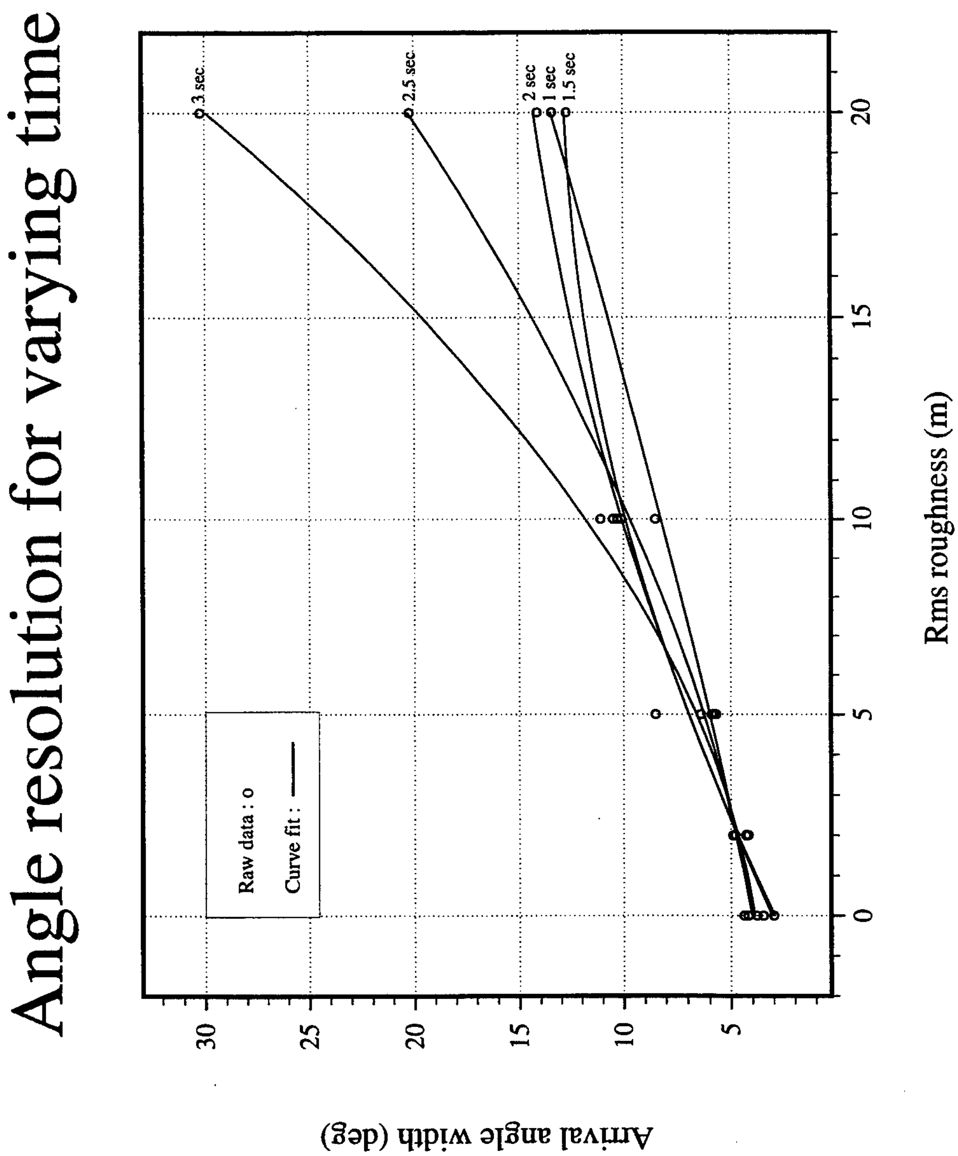

Figure 23. Angle width versus rms roughness for reduced time = 1, 1.5, 2, 2.5 and 3 second.

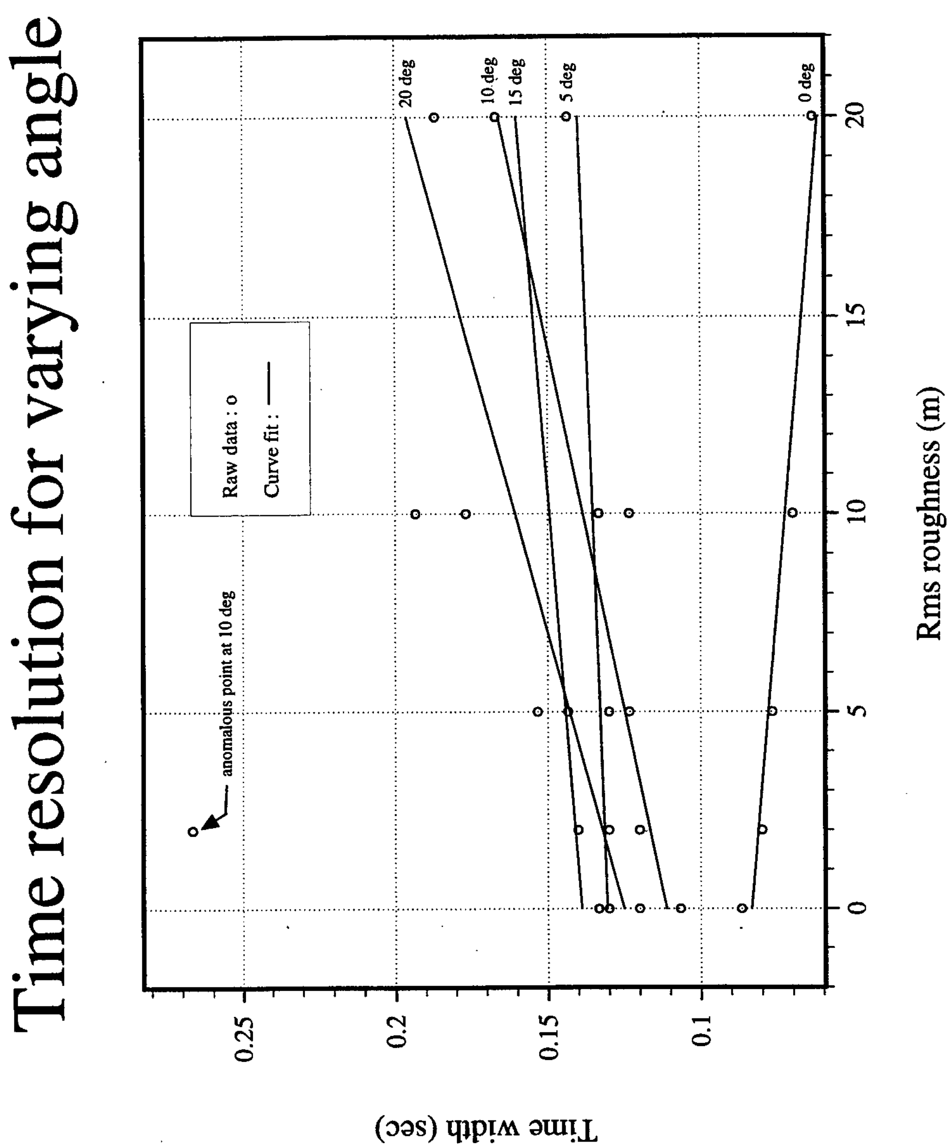

Figure 24. Time width versus rms roughness for arrival angle = 0, 5, 10, 15 and 20 degree.

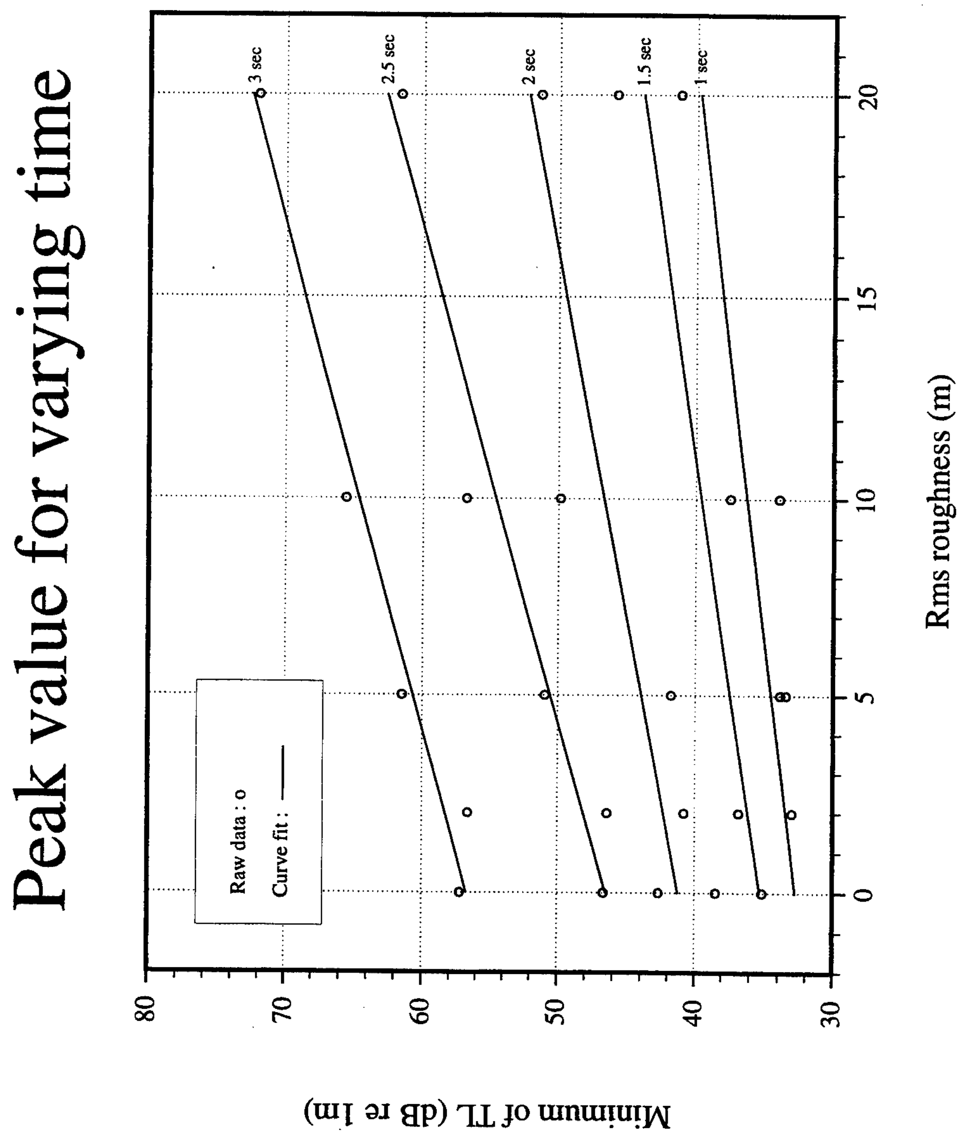

Figure 25. Peak minimum transmission loss versus rms roughness for reduced time = 1, 1.5, 2, 2.5 and 3 second.

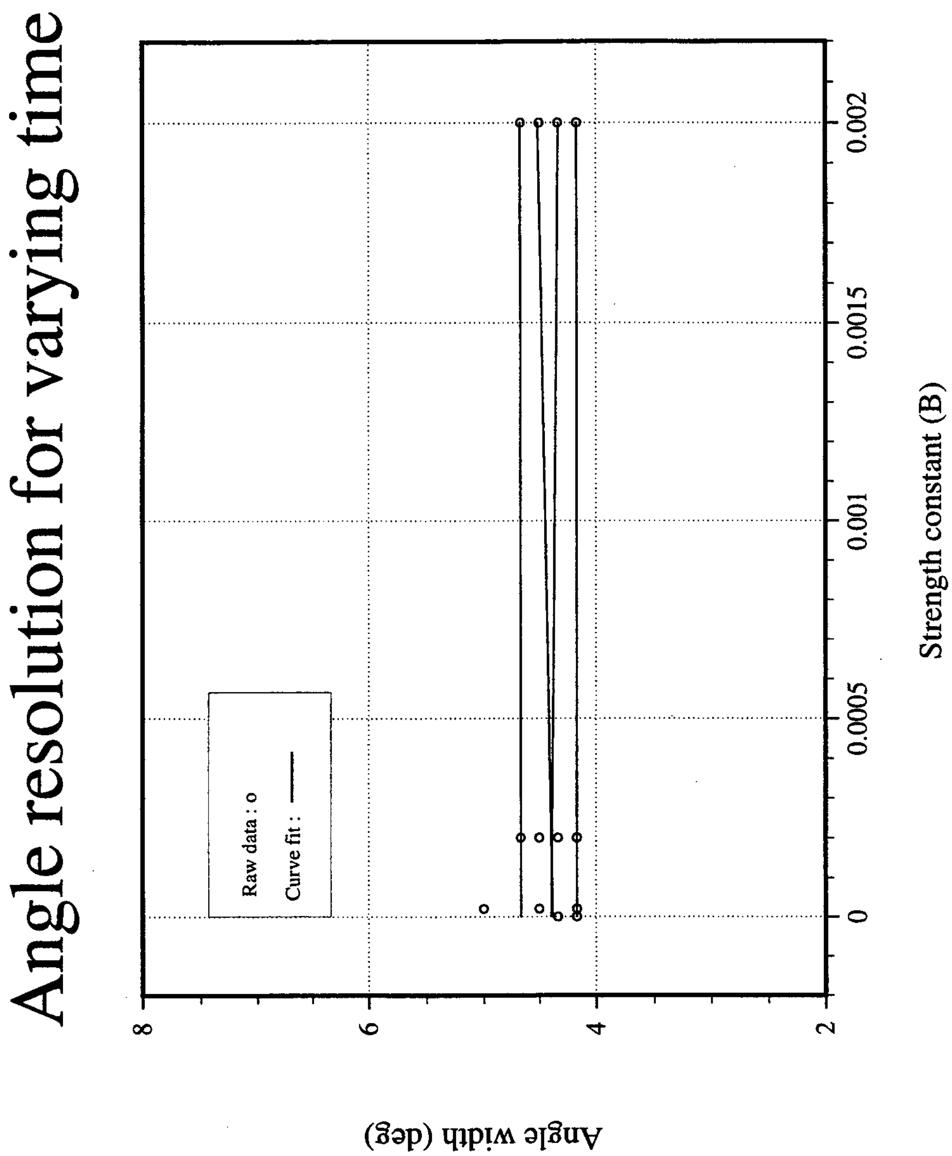

Figure 26. Angle width versus strength constant for reduced time = 1, 1.5, 2, 2.5 and 3 second.

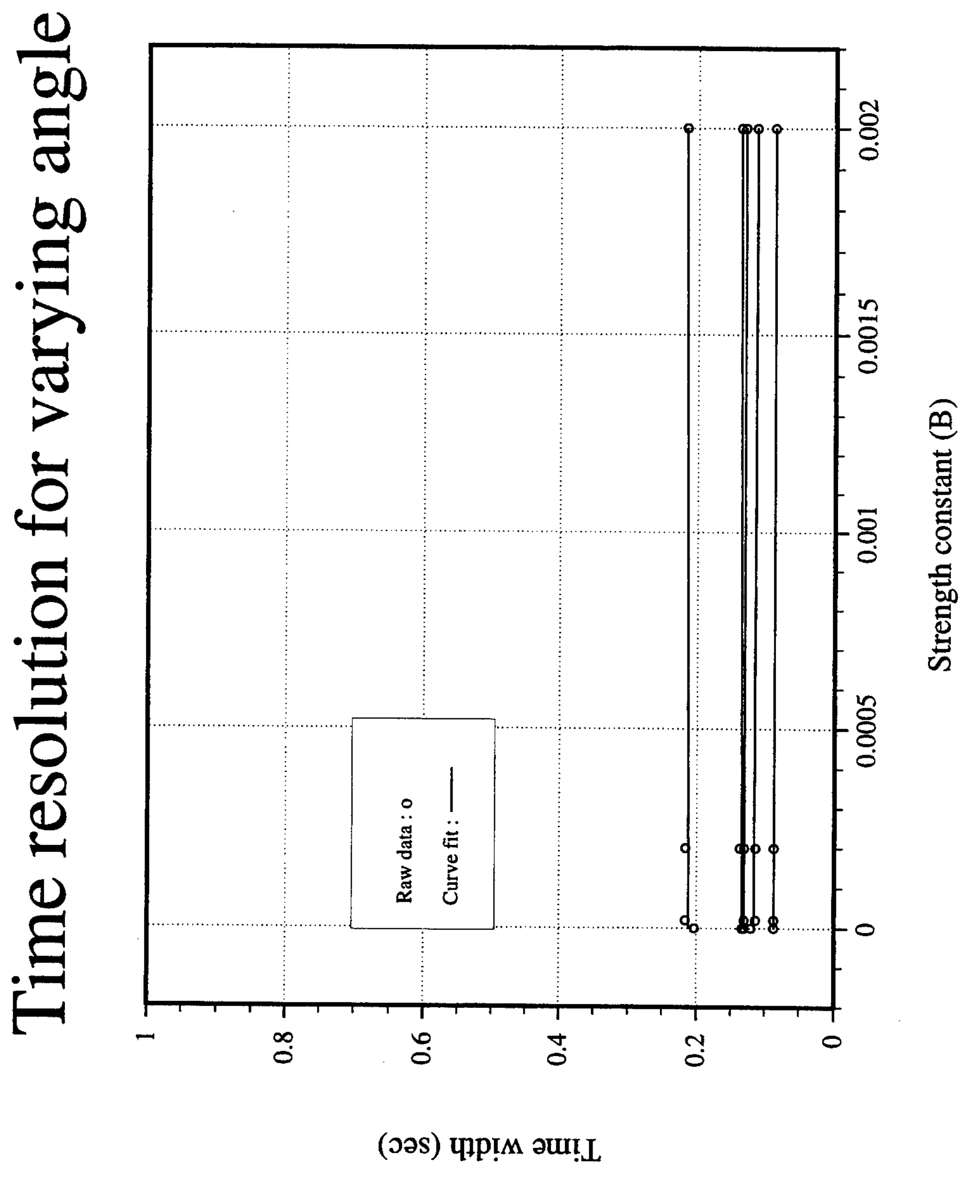

Figure 27. Time width versus strength constant for arrival angle = 0, 5, 10, 15 and 20 degree.

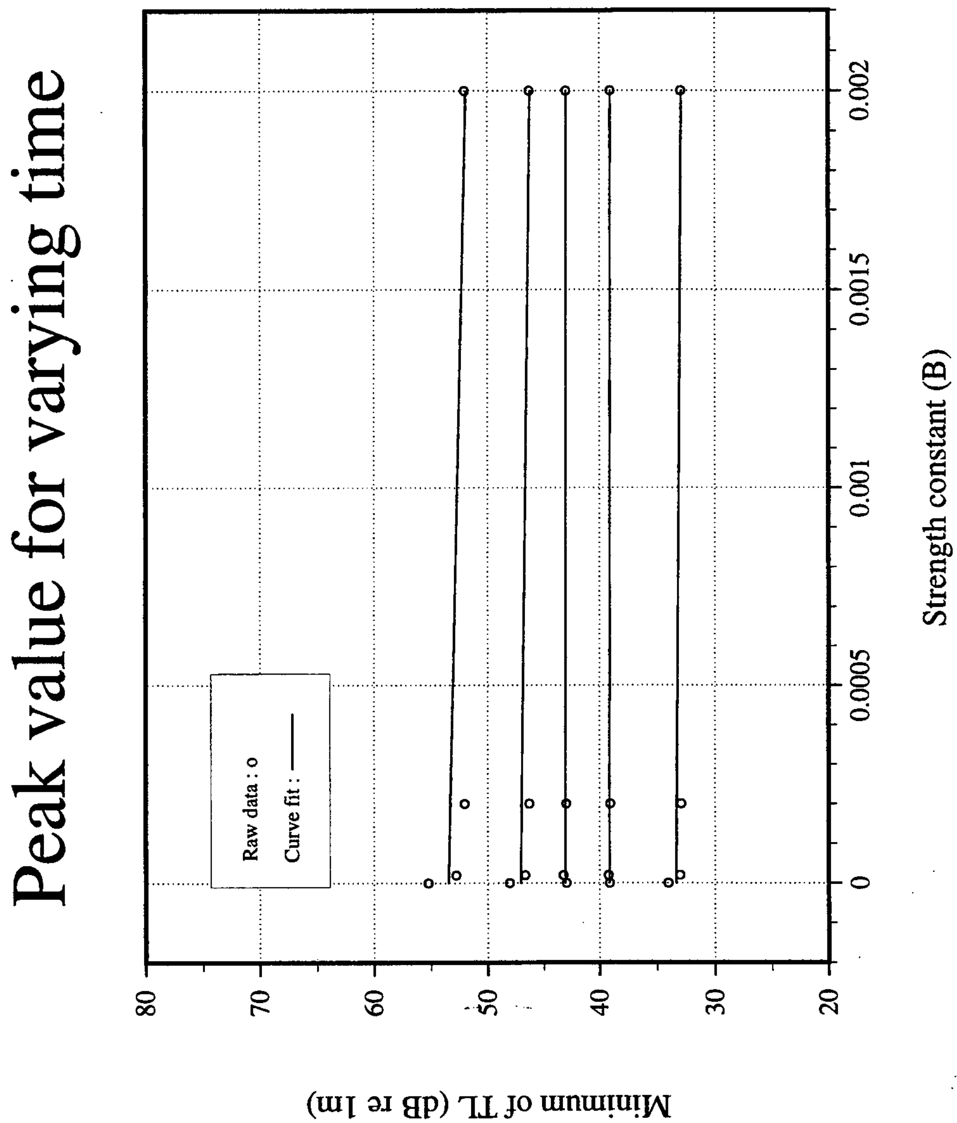

Figure 28. Peak minimum transmission loss versus strength constant for reduced time = 1, 1.5, 2, 2.5 and 3 second.

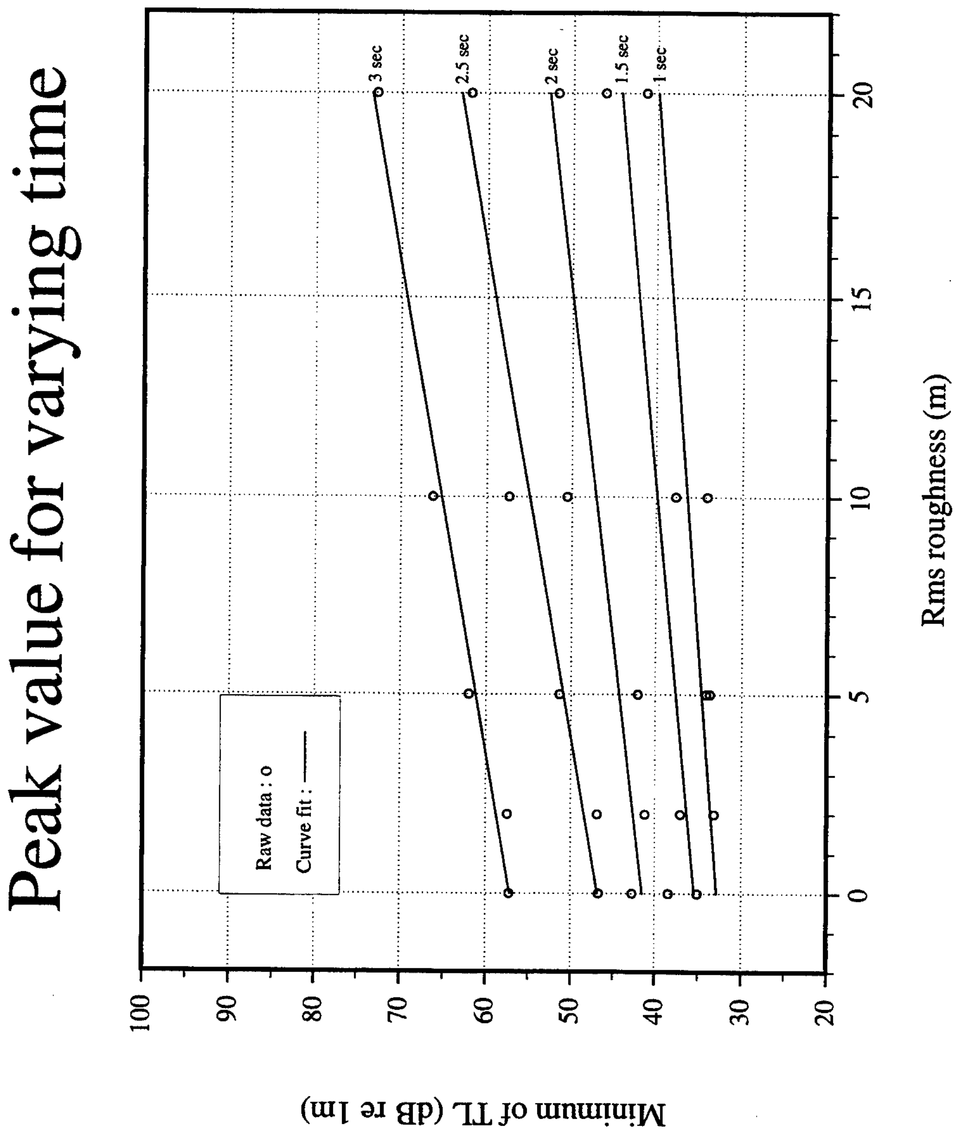

Figure 29. Peak minimum transmission loss versus rms roughness for reduced time = 1, 1.5, 2, 2.5 and 3 second combine with strength constant = $2x10^{-3}$ $m^{1-\beta}$.

IV. CONCLUSION

In this thesis, we have presented a numerical investigation of the effects of bottom interface roughness and sediment volume fluctuations on the resolution of broadband pulse propagation in a simple, shallow water environment. Predictions of the acoustic propagation were accomplished with a broadband, wide-angle parabolic equation model. Fluctuations of the bottom interface and volume were computed from realistic spectra characterizing each structure. The strength, or level of variability, of each was varied independently in order to determine the relative influence on pulse resolution.

To be consistent with measurement techniques employed in underwater acoustics experiments, a beamforming algorithm was written to discriminate vertical arrival angles as a function of arrival time. When no fluctuations were introduced, the solution to the range-independent problem was found to agree with a standard normal mode analysis. When fluctuations were introduced, the symmetrical arrival time pattern became distorted, indicating a degradation in the resolution of the pulse. Such degradations are expected to limit the ability of some operational naval systems.

When interface roughness was introduced, the results suggested that the main parameter influencing resolution was the ratio of rms roughness to correlation length. In other words, a high value of rms roughness does not independently imply a degradation in the pulse shape if the correlation length is quite large. Similarly, a relatively small rms roughness may still significantly affect pulse resolution if accompanied by a very small correlation length. In contrast, the largest realistic scales of volume fluctuations had little impact on the pulse shape. A combination of large volume fluctuations and various scales of rms interface roughness showed that degradations of pulse resolution are dominated by the interface structure. While it may be possible that a different environment (e.g., strongly downward refracting water column and upward refracting sediment) would increase the influence of sediment heterogeneity, such cases would also tend to increase interactions with the bottom interface resulting in similar conclusions.

An attempt was made to quantify these results by measuring the $1/e$ - width of the pulse at various arrival angles or arrival times as a function of the fluctuation strength. It was observed that an rms interface roughness of 10 m with a correlation length of 1000 m produced a doubling of the angular width of the arrivals and increased the transmission loss by as much as 10 dB. The time width was more stable, however. In none of the cases with volume fluctuations was the signal found to degrade appreciably. When the two influences were combined, the results were nearly identical to the case with no volume fluctuations.

Overall, these results suggest that bottom interactions in shallow water propagation are dominated by interface scatter. The degradation of pulse resolution depends on a combination of the rms interface roughness and an associated correlation length scale. In order to know á priori the limitations of pulse resolution, it is necessary to obtain an accurate statistical representation of the sea floor topography. In contrast, the sub-bottom volume fluctuations do not appear to significantly influence the forward propagation.

LIST OF REFERENCES

DeFotta, D. J., J. G. Lucas and N. S. Hodgkiss, *Digital Signal Processing: A System Design Approach*, p. 628-649, New York: John Wiley and Sons, 1988.

Etter, P. C., *Underwater Acoustic Modeling: Principles, Techniques and Applications*, New York: Elsevier Applied Science, 1991.

Hardin, R. H. and F. D. Tappert, "Applications of the Split-Step Fourier Method to the Numerical Solution of Nonlinear and Variable Coefficient Wave Equation," *SIAM Rev.* 15, 1973.

Jackson, D. R. and K. B. Briggs, "High-frequency Bottom Backscattering: Roughness Versus Sediment Volume Scattering," *The Journal of the Acoustical Society of America*, vol. 92, pp. 962-977, 1992

Jensen, F. B. and W. A. Kuperman, "Optimum Frequency of Propagation in Shallow Water Environments," *The Journal of the Acoustical Society of America*, vol. 73:3, pp. 813-818, 1983.

Smith, K. B, and F. D. Tapper, "UMPE: The University of Miami Parabolic Equation Model Version 1.1," MPL Technical Memorandum 432, San Diego, California, 1994.

Smith, K. B., M. G. Brown and F. D. Tappert, "Ray Chaos in Underwater Acoustics," *The Journal of the Acoustical Society of America*, vol. 91, pp. 1939-1949, 1992.

Tappert, F. D., "Parabolic equation method in underwater acoustics," *The Journal of the Acoustical Society of America*, Supplement vol. 55,S34, 1974.

Tappert, F. D., "The parabolic approximation method," in Lecture Note in Physics, vol. 70, Wave Propagation and Underwater Acoustics, p.224-287, New York: Springer-Verlag, 1977.

Thomson, D. J. and N. R. Chapman, "A wide-angle split-step algorithm for the parabolic equation," *The Journal of the Acoustical Society of America*, vol. 74, p1848-1854, 1983.

Thomson, D. J. and C. S. Bohun, "A Wide-angle Initial Field for the Parabolic Equation Models," The Journal of the Acoustical Society of America. Supplement vol. 83, S118, 1988.

Yamamoto, T., "Velocity Variabilities and other Physical Properties of Marine Sediments Measured by Crosswell Acoustic Tomography", *The Journal of the Acoustical Society of America*, vol. 98:4, p. 2235-2248, 1995.

Ziomek, L. J., *Fundamentals of Acoustic Field Theory and Space-Time Signal Processing*, Florida: CRC Press, Inc., 1995.

INITIAL DISTRIBUTION LIST

		No. Copies
1.	Defense Technical Information Center 8725 John J. Kingman Rd., STE 0944 Ft. Belvoir, Virginia 22060-6218	2
2.	Dudley Knox Library Naval Postgraduate School 411 Dyer Rd. Monterey, California 93943-5101	2
3.	Professor Kevin B. Smith, Code PH/Sk Department of Physics Naval Postgraduate School Monterey, California 93943-5101	3
4.	Professor Anthony A. Atchley, Code PH/Ay Department of Physics Naval Postgraduate School Monterey, California 93943-5101	1
5.	Dr. Jeff Simmen (Code 321 OA) Office of Naval Research 800 North Quincy Street Arlington, VA 22217	1
6.	Dr. Ellen Livingston (Code 321 OA) Office of Naval Research 800 North Quincy Street Arlington, VA 22217	1
7.	MAJ Hsiao-tseng Lin SGC #2552 NPS Monterey, California 93943-5000	1
8.	LT Ming-fei Chuang SGC #1234 NPS Monterey, California 93943-5000	1

9. LCDR Mei-chun Yuan 3
5th, 26, Lane 220, Te-hsien Rd.
Nan-tsu, Kaohsiung, Taiwan R.O.C.

10. Library of Chung Cheng Institute of Technology 1
P.O. Box 90047, Ta-hsi
Taoyuan, Taiwan R.O.C.